Editors' Suggestion

# Strain- and confinement-induced topological phases in noncentrosymmetric wurtzite HgTe

Antoine Hage [1], Jing Li [2,*] and Christophe Delerue [1,†]
[1] *Univ. Lille, CNRS, Univer. Polytechnique Hauts-de-France, Junia, UMR 8520—IEMN—Institute of Electronics Microelectronics and Nanotechnology, F-59000 Lille, France*
[2] *Univ. Grenoble Alpes, CEA, Leti, F-38000 Grenoble, France*

(Received 12 April 2026; accepted 20 July 2026; published 16 September 2026)

While three-dimensional Dirac semimetals have been extensively studied in centrosymmetric materials such as $Cd_3As_2$ and $Na_3Bi$, the recent colloidal synthesis of wurtzite HgTe (wz-HgTe) opens new opportunities for exploring topological quantum phases in noncentrosymmetric systems. Building on recent evidence that bulk wz-HgTe is a noncentrosymmetric Dirac semimetal, we investigate how strain and quantum confinement reshape its topology. To this end, we combine *ab initio* density-functional theory, semiempirical tight-binding, and $\mathbf{k}\cdot\mathbf{p}$ approaches. Bulk wz-HgTe hosts two Dirac points along the Γ–A line, i.e., along the *c* axis, located only 37 meV above the Fermi level, indicating that the Dirac regime should be experimentally accessible by doping or electrostatic gating. We show that biaxial strain drives a sequence of topological phase transitions from a Dirac semimetal to a three-dimensional topological insulator and eventually to a multiband metal. In (0001) thin films, quantum confinement induces oscillatory transitions between trivial and topological insulating phases. We demonstrate that this behavior is governed not only by the underlying *s*–*p* band inversion, but also by the crystal-field splitting specific to the wurtzite structure and by the presence of bulk Dirac points. In contrast, $(1\bar{1}00)$ films exhibit a single topological transition and, above a critical thickness, develop surface states forming Fermi-arc-like contours that connect the projections of the Dirac points in the two-dimensional Brillouin zone. In the same weak-confinement regime, semimetallic nanowires oriented along the *c* axis are predicted to host localized edge states that should be accessible to transport measurements or scanning tunneling spectroscopy. These results establish the topological phase diagram of wz-HgTe beyond the strong-confinement regime explored so far and reveal how crystal symmetry, inversion breaking, strain, and confinement combine to reshape the topology of a Dirac material. More broadly, they identify wurtzite HgTe as a promising platform for engineering topological phases in experimentally relevant nanostructures.

DOI: 10.1103/5pj7-34v4

## I. INTRODUCTION

Three-dimensional (3D) Dirac semimetals (DSMs) have attracted considerable interest in condensed-matter physics because they host fourfold-degenerate Dirac points, around which the electronic bands disperse linearly along the three directions of reciprocal space [1,2]. These materials are often viewed as 3D counterparts of graphene [3] and of the Dirac surface states of topological insulators [4,5]. Theoretical [2,6] and experimental [7–13] studies have established $Cd_3As_2$ and $Na_3Bi$ as prototypical examples of this class of quantum matter.

DSMs can be broadly divided into two categories [14,15]. In the first, crystal symmetry enforces the presence of Dirac points at high-symmetry points of the Brillouin zone [1]. In the second, often referred to as topological DSMs, the Dirac points arise from an inversion between valence and conduction bands and are protected by rotational symmetry along a high-symmetry axis [2]. In such systems, the Dirac points are constrained to lie on the rotation axis, although their precise position is not fixed *a priori*. The linear crossing is allowed because the bands involved belong to different irreducible representations along this axis. $Cd_3As_2$ and $Na_3Bi$ belong to this second class and have motivated a broad theoretical framework for symmetry-protected Dirac semimetals [14].

As in topological insulators [16], the electronic topology of DSMs can be profoundly modified by perturbations such as alloying, strain, electric fields, or quantum confinement [2,6,17]. In particular, the dimensional crossover from three dimensional to two dimensional (2D) provides access to a wide variety of topological phases that depend on film thickness, crystallographic orientation, and electrostatic environment, as shown for $Na_3Bi$ [2,18–20] and $Cd_3As_2$ [21–23] thin films. These examples illustrate that the topology of a Dirac material is not only a bulk property, but also a sensitive function of reduced dimensionality and symmetry breaking.

Breaking inversion symmetry in a centrosymmetric topological DSM can, in principle, split each Dirac point into

*Contact author: jing.li@cea.fr
†Contact author: christophe.delerue@iemn.fr

two Weyl points of opposite chirality [2,9,14,24]. In Weyl semimetals, these topological charges protect open surface states in momentum space, the so-called Fermi arcs [25]. Such states have been observed in several noncentrosymmetric Weyl materials, including TaAs [26,27], TaP [28], NbAs [29], and NbP [30]. In contrast, surface states in Dirac semimetals are generally more subtle: They need not be topologically protected and may instead appear as closed or deformed Fermi-arc-like features [15,31]. Understanding how such states evolve in systems where inversion symmetry is absent from the outset therefore remains an important open problem.

In this perspective, noncentrosymmetric topological DSMs are particularly appealing. They retain symmetry-protected Dirac points despite the absence of inversion symmetry, but remain much less explored than their centrosymmetric counterparts [32]. A few candidates have been proposed on the basis of *ab initio* calculations [17,32,33], yet the broader consequences of inversion breaking for strain-tunable topology, reduced dimensionality, and surface-state formation are still largely unexplored.

In this work, we focus on mercury telluride, a semimetal whose zinc-blende phase (zb-HgTe) has played a central role both in infrared optoelectronics [34] and in the development of topological condensed-matter physics through quantum-confined [35] and strain-induced [36] topological phases. Recently, colloidal synthesis of HgTe in the noncentrosymmetric wurtzite phase (wz-HgTe) has been achieved [37], opening access to an experimentally realized material platform in which band inversion and inversion breaking coexist.

Recent experimental and theoretical work [38] has established metastable wz-HgTe nanostructures and identified bulk wz-HgTe as a noncentrosymmetric topological Dirac semimetal. In the bulk, two Dirac points occur along the Γ–A line at $(0, 0, \pm k_D)$, with $k_D = 0.0255$ Å$^{-1}$, and lie only 37 meV above the Fermi level of the neutral system. This small energy offset suggests that the Dirac regime should be experimentally accessible by $n$-doping or electrostatic gating. The nanorods studied so far, however, have transverse dimensions of only a few nanometers and therefore belong to the strong-confinement regime, in which the confinement gap is much larger than the low-energy scale associated with the bulk Dirac points. The aim of the present work is therefore not to reestablish the bulk Dirac-semimetal phase, but to determine how strain and reduced dimensionality reshape this phase beyond the strong-confinement limit. Here, we refer to the weak-confinement regime as the range of larger characteristic dimensions, typically of order 10 nm or more, where the length scale $L_D = \pi/k_D \simeq 12$ nm becomes relevant and the projected or quantized bulk Dirac points control the low-energy topology.

More specifically, we show that wurtzite HgTe realizes a distinct topological setting in which the inverted $s$–$p$ band ordering of HgTe combines with the crystal-field splitting specific to the hexagonal wurtzite structure. This interplay qualitatively modifies the confinement-induced topological behavior compared with zb-HgTe and with more familiar centrosymmetric DSMs. Under biaxial strain in the $x$–$y$ plane, i.e., perpendicular to the $c$ axis, bulk wz-HgTe undergoes a sequence of phase transitions from a Dirac semimetal to a 3D topological insulator and eventually to a multiband metal. Under confinement along the $c$ axis, (0001) quantum wells develop a finite gap and alternate between 2D topological-insulator and trivial-insulator phases, with higher-order transitions that are directly tied to the wurtzite crystal field and to the presence of bulk Dirac points. In contrast, $(1\bar{1}00)$ thin films undergo a single topological transition and, above a critical thickness, develop surface states forming Fermi-arc-like contours that connect the projections of the two Dirac points in the 2D Brillouin zone. In the same weak-confinement regime, semimetallic nanowires oriented along the $c$ crystallographic axis host quantized edge subbands derived from these surface states, which evolve toward a quasicontinuous spectrum as the nanowire diameter increases.

The central question of this work is how the bulk Dirac-semimetal phase of noncentrosymmetric wz-HgTe evolves under two experimentally relevant perturbations: strain and quantum confinement. Biaxial strain tunes the relative ordering of the Γ-derived bands while preserving the rotational symmetry protecting the Γ–A Dirac points. Quantum confinement, in contrast, projects or quantizes the momentum along selected directions, so that the resulting topology depends strongly on whether the confinement direction is parallel or perpendicular to the Dirac-point axis. This provides the common framework for the strain, thin-film, and nanowire results discussed below.

The paper is structured as follows. The methodology of the electronic-structure calculations, combining *ab initio* density-functional theory (DFT), semiempirical tight-binding (TB), and $\mathbf{k}\cdot\mathbf{p}$ approaches, is described in Sec. II. The results for bulk wz-HgTe are presented in Sec. III, those for strained wz-HgTe in Sec. IV, those for thin films in Sec. V, and those for nanowires in Sec. VI.

## II. METHODOLOGY

### A. *Ab initio* calculations

*Ab initio* calculations were performed using the projector augmented-wave method [39] and a plane-wave cutoff energy of 400 eV. Spin-orbit coupling was included throughout. The Brillouin zone was sampled with a Γ-centered $6 \times 6 \times 4$ $k$-mesh. Electronic self-consistency was reached with an energy criterion of $10^{-8}$ eV, while structural relaxations were carried out using the Perdew–Burke–Ernzerhof (PBE) functional [40] with a convergence threshold of $10^{-5}$ eV. The electronic structure was further refined using the Heyd–Scuseria–Ernzerhof (HSE06) hybrid functional [41]. All calculations were performed with vasp [42–45]. Irreducible representations were identified using irvsp [46], following the Cracknell–Davies–Miller–Love (CDML) notation [47] implemented on the Bilbao Crystallographic Server [48]. Wannier models [49] were generated from the HSE results using Wannier90 [50], with Hg $s, d$ and Te $s, p$ orbitals as projectors, and were used for the analysis of the bulk band structure. The accuracy of the Wannier model is shown in Appendix A by comparing directly with band structure using HSE06 functional, which was obtained by adding the $k$-points along

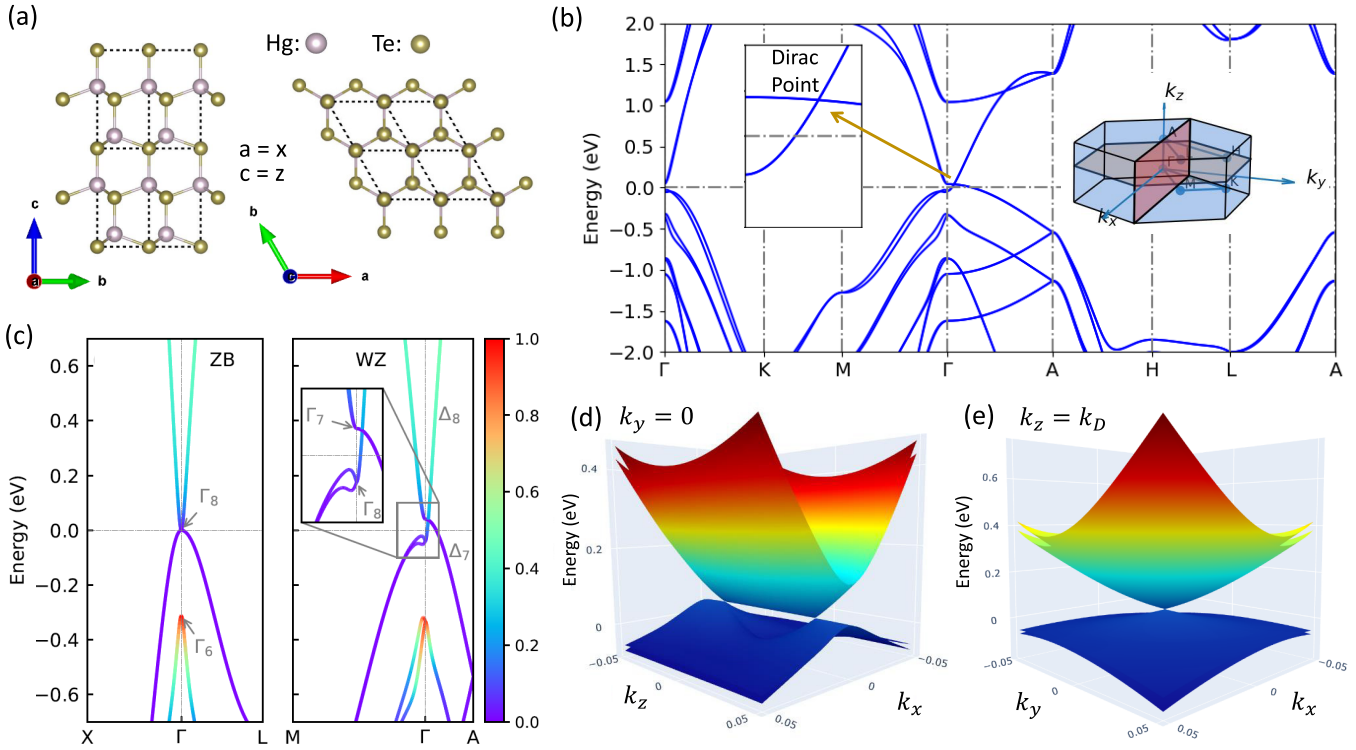


FIG. 1. (a) Atomic structure of wz-HgTe in the $y$–$z$ plane (left) and the $x$–$y$ plane (right). The unit cell is outlined by dotted boxes, with lattice vectors $a$, $b$, and $c$. In Cartesian coordinates, $a$ corresponds to $x$ and $c$ to $z$. (b) Bulk band structures of wz-HgTe obtained using a Wannier model based on *ab initio* HSE calculations. The Dirac point appears along Γ–$A$, as shown in the left inset. The band structure path is illustrated in the Brillouin zone (right inset). To confirm that the crossing is a Dirac point rather than a nodal line, 3D plots are provided: (d) in the $k_x$–$k_z$ plane at $k_y = 0$, showing two Dirac points at $\pm k_D$; and (e) in the $k_x$–$k_y$ plane at $k_z = k_D$, showing a single point crossing. (c) Comparison of zb-HgTe (left, along $X$–Γ–$L$) and wz-HgTe (right, along $M$–Γ–$A$) using TB models. The line colors represent the weight of $s$-orbital contributions from Hg and Te atoms.

high-symmetry lines as zero-weight points in the HSE06 calculations. These points do not contribute to the Brillouin-zone integration but provide explicit HSE eigenvalues along the band paths, including the Γ–A direction where the Dirac point occurs. For strained bulk calculations, ionic relaxations were performed at fixed strained lattice parameters for each strain value before the HSE06 electronic-structure calculation.

### B. Tight-binding calculations

In addition to *ab initio* calculations, we have developed a TB model for bulk wz-HgTe. This type of model is particularly effective for describing the electronic structure of spatially confined systems, such as quantum wells, quantum dots, and colloidal nanocrystals [51]. Unlike an *ab initio* approach based on Wannier functions, the semiempirical TB model provides a simplified description of surface passivation—particularly ligands in colloidal systems—which eliminate surface states associated with dangling bonds. This method therefore offers increased transferability to various types of synthesizable nanostructures and heterostructures, while maintaining sufficient accuracy for the analysis of electronic properties.

The electronic structure of wz-HgTe is calculated in TB as described in Ref. [52] for silicon. The Hamiltonian matrix is written in a basis of atomic orbitals that are assumed to be orthogonal. The Hamiltonian is expressed in terms of parameters adjusted to produce the optimal band structure, as compared with *ab initio* HSE calculations. Since a minimal set of $sp^3$ atomic orbitals and interactions limited to nearest neighbors are insufficient to accurately describe the conduction band [51–53], we therefore considered a basis of $sp^3d^5s^*$ orbitals ($s^*$ being a second $s$ orbital) and hopping terms limited to first neighbors [53,54]. Spin-orbit coupling is also included for the $p$ orbitals. The TB parameters are presented in Appendix B.

### C. k · p model

The **k** · **p** Hamiltonian is determined following the methodology detailed in Appendix C. The relevant physical description of the electronic structure near Dirac points requires the inclusion of at least six Bloch states at the Γ point [those shown in Fig. 1(c)]. They include the $p$ states of symmetry $\Gamma_7$ with energy $\varepsilon_p^+$, the $p$ states of symmetry $\Gamma_8$ with energy $\varepsilon_p^-$, and the $s$ states of symmetry $\Gamma_6$ with energy $\varepsilon_s$, all twice degenerate. The $6 \times 6$ matrix of the **k** · **p** Hamiltonian is written by arranging these states into two symmetrical blocks by reversing time:

$$H(\mathbf{k}) = \begin{pmatrix} H_{11}(\mathbf{k}) & H_{12}(\mathbf{k}) \\ H_{21}(\mathbf{k}) & H_{22}(\mathbf{k}) \end{pmatrix}, \tag{1}$$

with

$$H_{11}(\mathbf{k}) = \begin{pmatrix} \varepsilon_p^+ + (C_0^\parallel - D_p^+)k_\parallel^2 + (C_0^z - C_p^+)k_z^2 & Pk_+ & Qk_+ \\ Pk_- & \varepsilon_p^- + (C_0^\parallel - D_p^-)k_\parallel^2 + (C_0^z - C_p^-)k_z^2 & -iAk_z \\ Qk_- & iAk_z & \varepsilon_s + (C_0^\parallel + D_s)k_\parallel^2 + (C_0^z + C_s)k_z^2 \end{pmatrix}, \tag{2}$$

$$H_{22}(\mathbf{k}) = \begin{pmatrix} \varepsilon_p^+ + (C_0^\parallel - D_p^+)k_\parallel^2 + (C_0^z - C_p^+)k_z^2 & -Pk_- & -Qk_- \\ -Pk_+ & \varepsilon_p^- + (C_0^\parallel - D_p^-)k_\parallel^2 + (C_0^z - C_p^-)k_z^2 & -iAk_z \\ -Qk_+ & iAk_z & \varepsilon_s + (C_0^\parallel + D_s)k_\parallel^2 + (C_0^z + C_s)k_z^2 \end{pmatrix}, \tag{3}$$

and

$$H_{12}(\mathbf{k}) = \begin{pmatrix} 0 & 0 & 0 \\ 0 & iRk_+ & iSk_+ \\ 0 & iSk_+ & -iTk_+ \end{pmatrix}, \tag{4}$$

$$H_{21}(\mathbf{k}) = \begin{pmatrix} 0 & 0 & 0 \\ 0 & -iRk_- & -iSk_- \\ 0 & -iSk_- & iTk_- \end{pmatrix}, \tag{5}$$

with $k_\pm = k_x \pm ik_y$. The off-diagonal blocks $H_{12}$ and $H_{21}$ are symmetry allowed in the noncentrosymmetric wurtzite structure and are responsible for spin splittings away from the Γ–A axis. They are retained in the full $\mathbf{k}\cdot\mathbf{p}$ Hamiltonian. For the restricted analysis along Γ–A, however, $k_x = k_y = 0$, so that $k_\pm = 0$ and these blocks vanish identically. We also use the block-diagonal form $H_{12} = H_{21} = 0$ as a simplified model when discussing the one-dimensional (1D) $k_z$-dependent mechanism of the (0001) film transitions; the validity of this simplification for the low-energy dispersion is illustrated in Fig. 8. The various parameters of the $\mathbf{k}\cdot\mathbf{p}$ model are given in Appendix C.

## III. BULK BAND STRUCTURE

The bulk Dirac-semimetal character of wz-HgTe, including the *s*–*p* band inversion and the existence of Dirac points along Γ–A, was established in Ref. [38]. Here, we briefly recall only the bulk features that are needed to analyze the strain- and confinement-induced phases discussed in the following sections. We adopt the experimental lattice parameters of bulk wz-HgTe, $a_0 = 4.546$ Å and $c_0 = 7.535$ Å, from Ref. [37]. After structural relaxation, we obtain an anion internal parameter of $u = 0.3719$ for bulk wz-HgTe, whose unit cell is shown in Fig. 1(a).

Figure 1(b) presents the electronic band structure of wz-HgTe calculated within DFT using the HSE hybrid functional. Along the Γ–A direction, one observes a crossing between a strongly dispersive doubly degenerate band and a relatively flat doubly degenerate band. The crossing is not part of a nodal line but remains a single point in the $k_x$–$k_y$ plane, where it exhibits a fourfold degeneracy, thus identifying it as a Dirac point, as confirmed in Fig. 1(e). Two such Dirac points are located symmetrically in the Brillouin zone at $(0, 0, \pm k_D)$, with $k_D = 0.0255$ Å$^{-1}$, where the $z$ axis coincides with the crystallographic $c$ axis of the wurtzite lattice. Their local dispersion in the $k_x$–$k_z$ plane at $k_y = 0$ is shown in Fig. 1(d). These Dirac points lie close to the Γ point.

Although wz-HgTe lacks inversion symmetry, the two crossing bands remain doubly degenerate along the Γ–A axis. This double degeneracy is protected by the sixfold rotational symmetry of the crystal [32]. Moreover, the crossings at $k_z = \pm k_D$ are symmetry protected because the two bands belong to different irreducible representations, $\Delta_7$ and $\Delta_8$, along this high-symmetry line. Consequently, the Dirac points remain robust as long as the rotational symmetry is preserved (see Sec. IV). The bands also exhibit an approximately linear dispersion in the vicinity of the crossing, consistent with the Dirac nature of these states.

The TB band structure is in excellent agreement with the HSE results over a broad energy range and throughout the Brillouin zone (Appendix B). This agreement is particularly accurate in the low-energy region around the Fermi level, including the exact position of the Dirac crossing at $k_D$. Such consistency demonstrates the transferability of the bulk TB parameters to reduced-dimensional systems, including thin films and nanostructures. It also provides a firm basis for constructing the effective $\mathbf{k}\cdot\mathbf{p}$ model derived in Appendix C, which reproduces the low-energy electronic structure using a reduced six-dimensional Hamiltonian while retaining the essential physics of the system.

The TB results further show that the *s*–*p* band inversion persists in wz-HgTe, as illustrated in the right panel of Fig. 1(c). However, in the wurtzite phase, the asymmetric crystal field lifts the fourfold degeneracy of the $\Gamma_8$-derived states and splits them into two distinct doubly degenerate bands. The Dirac points then emerge from the crossing of these split inverted bands, which is a characteristic consequence of the reduced symmetry of the wurtzite structure. It is worth noting that, in the neutral system, the Fermi level does not coincide exactly with the Dirac points. Instead, it lies about 37 meV below them, at $k = 0$, approximately midway between the doubly degenerate $\Gamma_7$ and $\Gamma_8$ states.

For comparison, undoped zb-HgTe is a semimetal whose Fermi level lies exactly at the $\Gamma_8$ point, where two oppositely dispersing bands meet to form a fourfold-degenerate state, as shown in the left panel of Fig. 1(c). These states are predominantly of *p*-orbital character, with a small admixture of *d* orbitals. The next lower valence band at Γ is the $\Gamma_6$ state, which is mainly of *s*-orbital character. In contrast to conventional semiconductors, the order of the $\Gamma_8$ and $\Gamma_6$ states

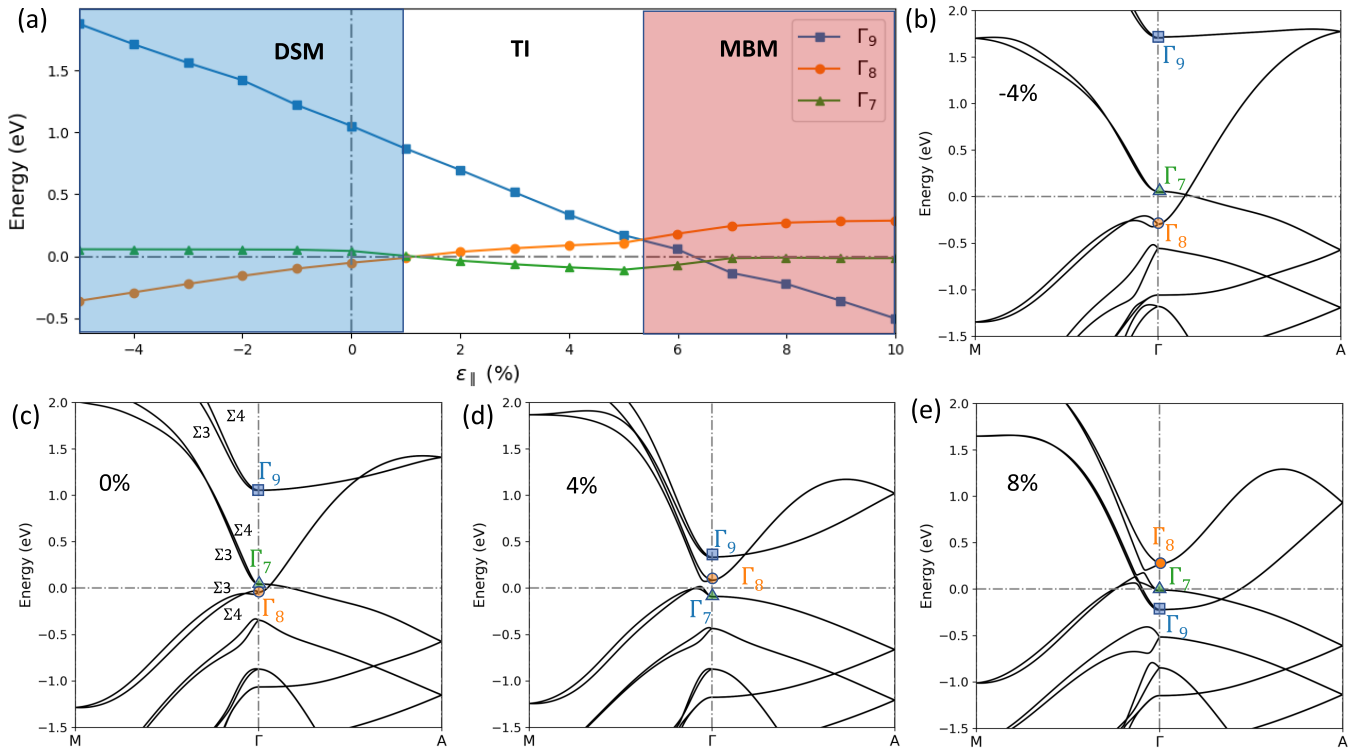


FIG. 2. (a) Position of $\Gamma_7$, $\Gamma_8$, and $\Gamma_9$ with respect to the Fermi level as a function of biaxial strain in the $x$–$y$ plane. The Dirac semimetal, topological insulator, and multiband metal phases are shaded in blue, white, and red. (b)–(e) The bulk band structures of wz-HgTe obtained using a Wannier model based on *ab initio* HSE calculations for −4%, 0%, 4%, and 8% biaxial strain in $x$–$y$ plane, respectively. Panels (b) and (c) demonstrate DSM with Dirac point on the Γ–A path. Panel (d) shows a topological phase. (e) An example of multiband metal.

is inverted, giving rise to the well-known negative band gap. This band inversion underlies the nontrivial topological properties of zb-HgTe thin films and strained zb-HgTe [35,36].

This bulk electronic structure provides the reference point for the following sections, where we examine how the Dirac points and the associated band inversion evolve under biaxial strain and reduced dimensionality.

## IV. BAND STRUCTURE OF STRAINED wz-HgTe

We first examine how the bulk Dirac-semimetal phase evolves under biaxial strain, which preserves the $C_6$ symmetry but modifies the Γ-derived band ordering. Under a biaxial strain $\varepsilon_\parallel$, the lattice parameters are deformed:

$$a = a_0 \times (1 + \varepsilon_\parallel), \tag{6}$$

$$c = c_0 \times \left(1 - 2\varepsilon_\parallel \frac{C_{13}}{C_{33}}\right), \tag{7}$$

where $C_{13} = 356.2$ GPa and $C_{33} = 798.4$ GPa are the elastic constants computed from DFT, and the unstrained lattice parameters ($a_0$ and $c_0$) are reported in Sec. III. The internal atomic coordinates were then rerelaxed at fixed strained lattice parameters using the PBE functional. The HSE06 electronic-structure calculations were subsequently performed on these relaxed strained structures. Thus, the strained configurations used here are not obtained by a rigid deformation of the unstrained crystal; the internal atomic positions are optimized separately for each strain value. We note that the broad strain range considered here is intended to map the theoretical evolution of the electronic structure. In particular, the largest positive strains should be viewed as an extrapolated regime and may not be attainable in freestanding wz-HgTe without epitaxial, substrate-induced, or nanostructure stabilization.

Figure 2(c) shows the simplified band structure along the M–Γ–A path in the absence of biaxial strain. At Γ, the bands near the Fermi level are identified, from top to bottom, as $\Gamma_9$, $\Gamma_8$, and $\Gamma_7$. Along the Γ–A direction, these bands evolve into the corresponding irreducible representations $\Delta_9$, $\Delta_8$, and $\Delta_7$. In contrast, along the Γ–M direction, each band splits into two branches labeled $\Sigma_3$ and $\Sigma_4$. The $\Gamma_9$ band lies about 1.2 eV above the Fermi level.

Under negative biaxial strain [Fig. 2(b)], the $\Gamma_9$ and $\Gamma_8$ bands move farther away from $\Gamma_7$, while the band-inversion condition at Γ remains unchanged. As a result, a Dirac point persists along the Γ–A path, and negatively strained wz-HgTe remains in the DSM phase.

When positive biaxial strain is applied, the $\Gamma_8$ band shifts upward and crosses the $\Gamma_7$ band at $\varepsilon_\parallel \approx 1\%$. Along the Γ–A direction, the $\Delta_7$ and $\Delta_8$ bands no longer cross, leading to the opening of a global bulk gap [Fig. 2(d)]. Since wz-HgTe lacks inversion symmetry, the topological character of this gapped phase was determined from the Wilson-loop evolution of the Wannier charge centers using the HSE-based Wannier Hamiltonian. The $Z_2$ indices on the six time-reversal-invariant planes are 1, 0, 1, 0, 1, and 0 for $k_1 = 0, k_1 = 1/2, k_2 = 0, k_2 = 1/2, k_3 = 0$, and $k_3 = 1/2$, respectively. This gives a strong topological index $\nu_0 = 1$ and weak indices (000),

confirming that this gapped phase is a strong 3D topological insulator. The retained $s$–$p$ band inversion at $\Gamma$ provides the physical origin of this nontrivial topology.

For larger positive biaxial strain, the $\Gamma_9$ band moves downward and crosses the $\Gamma_8$ and $\Gamma_7$ bands. This produces multiple band crossings and Fermi pockets near the Fermi level, as reflected by the M–$\Gamma$ dispersion in Fig. 2(e). We therefore refer to this region as a multiband metal (MBM). This terminology does not exclude symmetry-allowed crossings along $\Gamma$–A at other energies; rather, it indicates that the system is no longer a clean Dirac semimetal with an isolated low-energy Dirac point, nor a fully gapped topological insulator. The evolution from Dirac semimetal to topological insulator and finally to multiband metal as a function of biaxial strain is summarized in Fig. 2(a).

Because biaxial strain preserves the rotational symmetry that protects the Dirac point, the DSM phase remains stable as long as this symmetry is maintained. In contrast, any strain that breaks the rotational symmetry removes the Dirac protection and can drive the DSM phase into a gapped phase, such as a TI.

## V. BAND STRUCTURE OF THIN FILMS

We next turn to quantum confinement, where the key issue is how the bulk Dirac points are projected into the 2D Brillouin zone. Reducing the dimensionality of the material through quantum confinement can not only open a gap in the band structure, but also drive topological phase transitions. In 2D films, the resulting phase depends primarily on two factors: the orientation of the confinement with respect to the axis connecting the Dirac points (here the $z$ axis) and the film thickness. Such effects have already been observed or predicted in centrosymmetric Dirac semimetals such as $Na_3Bi$ and $Cd_3As_2$. In the present work, we focus on films grown along the [001] and [1$\bar{1}$0] directions, i.e., with confinement parallel and perpendicular to the $z$ axis, respectively.

### A. (0001) films

For (0001) films, the two Dirac points of the bulk material are projected onto the $\overline{\Gamma}$ point of the 2D Brillouin zone of the film. In this configuration, the central question concerns the possibility of interpreting the effects of quantum confinement along the $z$ axis in a manner analogous to those observed in thin layers of zb-HgTe, where topological properties emerge from the inversion of the $s$–$p$ bands, associated with a negative band gap.

Figure 3 illustrates the evolution of the band structure as a function of thickness for films whose surfaces are terminated by Te atoms on both sides. Similar but distinct behaviors are obtained for Hg-Hg or Te-Hg terminations (see Appendix D). Like in zb-HgTe [35], the thinnest films behave like trivial insulators ($Z_2 = 0$). Consistently, the bottom of the conduction band has an $s$ character, while the top of the valence band is $p$ type (see Fig. 10 in Appendix D), similar to conventional III–V or II–VI semiconductors (with positive band gap). As the thickness increases, the gap closes and then reopens, signaling a band crossover and a transition to a quantum spin Hall (QSH) topological-insulator phase. After reaching a maximum, the gap decreases again, leading to a second transition to a trivial phase. The second topological transition occurs when the subbands—initially the second conduction subband and the second valence subband in the thinnest films—intersect. These oscillations between QSH and trivial phases, observed here, had been predicted theoretically for $Na_3Bi$ [2], $Cd_3As_2$ [6], $Bi_2Se_3$, and $Bi_2Te_3$ [16] films. Topological phase transitions are accompanied by a reversal of the orbital character ($s \leftrightarrow p$) of the bands defining the gap, which is particularly pronounced during the first transition. Thus, at 2.26 nm, the upper (lower) band has a predominantly $s(p)$ character at $\Gamma$, while at 2.63 nm, this hierarchy is reversed (Fig. 10 in Appendix D). Although this $s$–$p$ inversion persists for subsequent transitions at greater thicknesses, the $s$-orbital weight difference between the gap edge states gradually decreases with increasing thickness.

TABLE I. Critical thicknesses corresponding to the first and second topological transitions in (0001) wz-HgTe films depending on the surface terminations. Each transition is located between the two specified thicknesses.

| Termination | First transition (nm) | Second transition (nm) |
|---|---|---|
| Te-Te | 2.26–2.63 | 14.69–15.07 |
| Hg-Hg | 4.14–4.52 | 16.58–17.00 |
| Hg-Te | 4.04–4.42 | 16.48–16.89 |

The first topological transition at thickness $L_z^{(1)}$ depends strongly on the surface termination (see Table I). This sensitivity can be explained by the marked localization, near the surfaces, of the state with a strong $s$ character, which initially constitutes the conduction band before the transition. A similar phenomenon is observed in thin films of zb-HgTe [55], although these exhibit only a single topological transition—a notable contrast with our predictions for wz-HgTe (0001) wells. Indeed, the latter exhibit higher-order topological transitions ($L_z^{(n)}$ for $n > 1$), reflecting an oscillation of the $Z_2$ invariant with increasing thickness $L_z$, which is absent in (001) zb-HgTe films.

The full TB model provides the quantitative thin-film band structures and $Z_2$ indices. The following $\mathbf{k} \cdot \mathbf{p}$ (methodology in Sec. II C and Appendix C) analysis is introduced only to clarify the physical mechanism behind the oscillatory topological transitions. As a reminder, the $\mathbf{k} \cdot \mathbf{p}$ Hamiltonian is expressed in a basis of six Bloch states, the $p$ states of symmetry $\Gamma_7$ with energy $\varepsilon_p^+$, the $p$ states of symmetry $\Gamma_8$ with energy $\varepsilon_p^-$, and the $s$ states of symmetry $\Gamma_6$ with energy $\varepsilon_s$, all twice degenerate. At $k_x = k_y = 0$, the Hamiltonian breaks down into two spin-degenerate $3 \times 3$ blocks of the form

$$\begin{pmatrix} E_0(k_z) & 0 & 0 \\ 0 & \varepsilon_p^- - Mk_z^2 & -iAk_z \\ 0 & iAk_z & \varepsilon_s + Nk_z^2 \end{pmatrix}, \tag{8}$$

with a pure diagonal term $E_0(k_z) = \varepsilon_p^+ - Lk_z^2$ associated with the $p$ states from $\Gamma_7$. The $2 \times 2$ block describes the strong coupling ($\propto k_z$) between the $p$ states of $\Gamma_8$ and the $s$ states of $\Gamma_6$. The parameters in Eq. (8) are $\varepsilon_p^+ = 40.2$ meV, $\varepsilon_p^- = -39.7$ meV, $\varepsilon_s = -333.5$ meV, $A = 6.57$ eV Å, $L = 4.99$ eV Å$^2$, $M = 8.08$ eV Å$^2$, and $N = 54.12$ eV Å$^2$. If

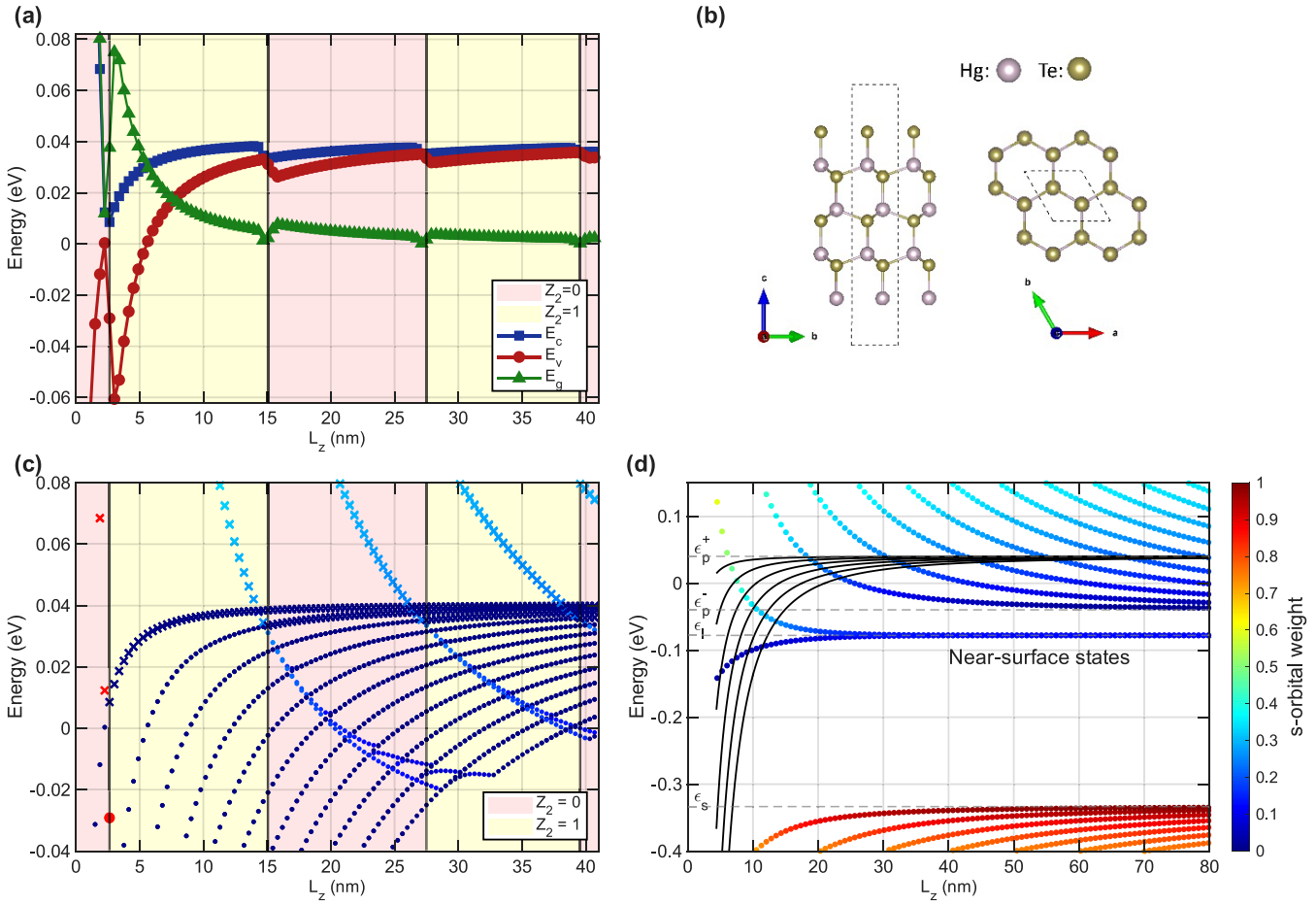


FIG. 3. Results for (0001) films terminated by Te on both sides. (a) Energy of band edges and band gap at $k_x = k_y = 0$ as a function of the film thickness $L_z$. The vertical lines indicate the transitions between topological phases, distinguishing between the trivial ($Z_2 = 0$, pink region) and nontrivial ($Z_2 = 1$, yellow region) regimes. (b) Film geometry and atomic positions in the $y$–$z$ plane (left) and the $x$–$y$ plane (right). (c) Energy of the lowest conduction and highest valence bands at $k_x = k_y = 0$ as a function of $L_z$, calculated using the TB model. The markers are colored according to the weight of the wave functions on the atomic $s$ orbitals. The vertical lines and background colors are identical to those in panel (a); crosses and points denote the edges of conduction and valence bands, respectively, these roles being reversed when valence and conduction bands intersect. (d) Electronic energy levels at $k_x = k_y = 0$ as a function of $L_z$ in the $\mathbf{k} \cdot \mathbf{p}$ model. The color mapping is the same as in panel (c). The solid lines correspond to purely $p$ states whose energy dispersion is given by $E_0(k_n)$, where $k_n = n\pi/L_z$, with $n = 1, 2, 3, 4, 5, 6$.

the eigenvalues of the $2 \times 2$ block are denoted by $E_\pm(k_z)$, the position $k_D$ of the Dirac point is given by the crossing between $E_0$ and $E_+$, which is protected by the $C_6$ symmetry. Setting $E_0(k_D) = E_+(k_D)$ gives $k_D = 0.0266\,\text{Å}^{-1}$, very close to the HSE or TB value.

The splitting $\varepsilon_p^+ > \varepsilon_p^-$ reflects the effect of the wurtzite crystal field, while the splitting $\varepsilon_p^- > \varepsilon_s$ reflects the inversion of $s$ and $p$ bands at $k_z = 0$. Nevertheless, examination of the diagonal terms of Eq. (8) shows that normal order is restored for $k_z > k_I$ such that $\varepsilon_p^- - Mk_I^2 = \varepsilon_s + Nk_I^2 = \varepsilon_I = -78$ meV. Based on these elements, two characteristic lengths can be introduced: $L_D = \pi/k_D = 11.9$ nm and $L_I = \pi/k_I = 4.6$ nm.

Following standard procedures, we express the electronic states of (0001) quantum wells as linear combinations of Bloch states, modulated by envelope functions that cancel at the interfaces and satisfy differential equations where the wave vector $k_z$ is replaced by the operator $-i\partial/\partial z$ [56]. The energy solutions at $k_x = k_y = 0$ are shown in Fig. 3(d). The $p$ states derived from the diagonal term of the Hamiltonian, whose envelope function is of the form $\sin(k_n z)$, with $k_n = n\pi/L_z$, have an energy $E_0(k_n)$ that converges to $\varepsilon_p^+$ for $L_z \to \infty$. The states derived from the $2 \times 2$ block of Eq. (8), determined numerically (Appendix D 4), fall into two categories. On the one hand, there are extended states, characteristic of quantum wells, forming multiple subbands. Their energy tends toward $\varepsilon_p^-$ for states of marked $p$ character (above $\varepsilon_p^-$) and toward $\varepsilon_s$ for those of $s$ character (below $\varepsilon_s$). On the other hand, calculations reveal the existence of a pair of localized states (each degenerate in spin) in the vicinity of each surface of the thin film. For thick films ($L_z \gg 20$ nm), their energy coincides with $\varepsilon_I$ (justification in Appendix D 5), the boundary energy of the $s$–$p$ inversion, located between $\varepsilon_p^-$ and $\varepsilon_s$. As the thickness decreases, the coupling between the states of opposite surfaces leads to the formation of a bonding state and an antibonding state. The latter, strongly $s$,

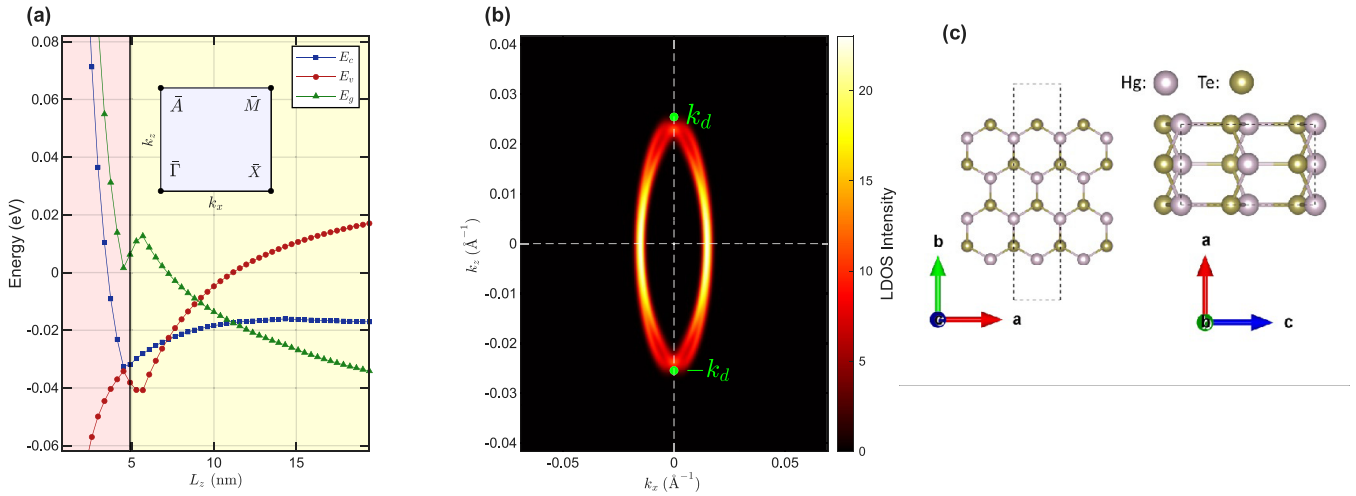


FIG. 4. Results for $(1\bar{1}00)$ films. (a) Energy of band edges and band gap as a function of the film thickness $L_z$. The vertical lines indicate the transitions between topological phases, distinguishing between the trivial ($Z_2 = 0$, pink region) and nontrivial ($Z_2 = 1$, yellow region) regimes. The colors are the same as in Fig. 3(a). A quarter of the 2D rectangular Brillouin zone is also displayed as an inset. (b) LDOS on surface atoms at the energy of the Dirac point ($E_D = 37$ meV) highlighting surface states forming Fermi-arc-like contours for a 23.0 nm thick slab. (c) Film geometry and atomic positions in the $x$–$y$ plane (left) and the $x$–$z$ plane (right). The structure is periodic along the $x$ and $z$ directions represented by vectors $a$ and $c$, respectively.

sees its energy increase to form the bottom of the conduction band in the thinnest films. The existence of this antibonding near-surface state is confirmed by TB calculations, although its $s$ character appears more pronounced, probably due to couplings not captured by the intrinsically limited $\mathbf{k} \cdot \mathbf{p}$ model. It should be noted that, for thick films, these near-surface states become difficult to detect in TB, buried within a high density of valence states.

The physical origin of the different topological transitions can be understood from Fig. 3(d). The first transition results from the crossover between the pure $p$ state of energy $E_0(k_1)$ and the antibonding near-surface state, marked by a strong $s$ character. The critical thickness $L_z^{(1)}$ at which this transition occurs depends on the surface passivation (in TB), due to the localized nature of the surface state. However, $L_I$ can be considered a rough approximation of this threshold ($L_z^{(1)} \approx L_I$).

The subsequent topological transitions arise from successive crossings between the states $E_0(k_n)$ for $n > 1$ and the quantized states converging toward $\varepsilon_p^-$. The latter have a residual $s$ component, which gradually decreases as the film thickness increases. These behaviors are in very good agreement with TB results (see the band structures in the vicinity of the topological transitions in Appendix D).

In Appendix D 6, we present a figure similar to Fig. 3(d), but obtained by imposing $\varepsilon_p^+ = \varepsilon_p^- = 0$, i.e., in the absence of crystal-field splitting characteristic of the wurtzite structure and, consequently, in the absence of Dirac points. This configuration is similar to that of zb-HgTe. In this case, the states $E_0(k_n)$ for $n > 1$ cannot cross any other states, since they all converge toward $\varepsilon_p^+ = \varepsilon_p^-$ from above and from below, respectively. Only the first topological transition remains, induced by the crossing with the antibonding near-surface state. This observation is confirmed by TB [55] and $\mathbf{k} \cdot \mathbf{p}$ [35] calculations on zb-HgTe quantum wells, which reveal only a single topological transition. We conclude that the topological transitions observed at thicknesses $L_z^n$ for $n > 1$ in wz-HgTe films are specific to this crystalline phase and are directly correlated with the presence of the two Dirac points along the $k_z$ axis. As confirmation, the distance $\Delta L_z = L_z^{n+1} - L_z^n$ between two topological transitions is remarkably constant (for $n > 1$) and very close to $L_D$.

### B. $(1\bar{1}00)$ films

$(1\bar{1}00)$ films exhibit markedly distinct behavior (Fig. 4). With the wurtzite $c$ axis confined to the film plane, the Dirac points project onto $\pm k_D$ along $k_z$ ($\bar{\Gamma}$–$\bar{A}$) in the 2D rectangular Brillouin zone. Like in the previous case and in zb-HgTe, the thinnest films exhibit a topologically trivial ($Z_2 = 0$) nonzero gap [Fig. 4(a)], though this gap does not occur at the $\Gamma$ point (see examples of band structures in Fig. 13 of Appendix E). The gap closes at a thickness of approximately 4.7 nm before reopening, marking a transition into a topological-insulator phase ($Z_2 = 1$), which persists for all thicker films studied (up to 20 nm). This single topological transition has the same physical origin as in zb-HgTe films, as well as the first topological transition in (0001) films of wz-HgTe. In support of this assertion, the diagonal energies of the $s$- and $p$-type sectors in the $\mathbf{k} \cdot \mathbf{p}$ model cross at $k \approx 0.098$ Å$^{-1}$ along the growth direction, yielding an estimated critical thickness of $\pi/k \approx 3.2$ nm. This rough estimate aligns with TB calculations.

Figure 4(a) and band structures provided in Appendix E show that films thicker than ≈7 nm become semimetallic: The valence band maximum rises above the conduction band minimum but at distinct $k$-points, without direct band crossing, which allows us to define the topology of the bands despite the negative gap.

To probe the topological effects on the electronic structure of $(1\bar{1}00)$ thin films, we computed the surface local density of states (LDOS) as a function of the in-plane wave vectors. Our calculations reveal the emergence of two Fermi-arc-like

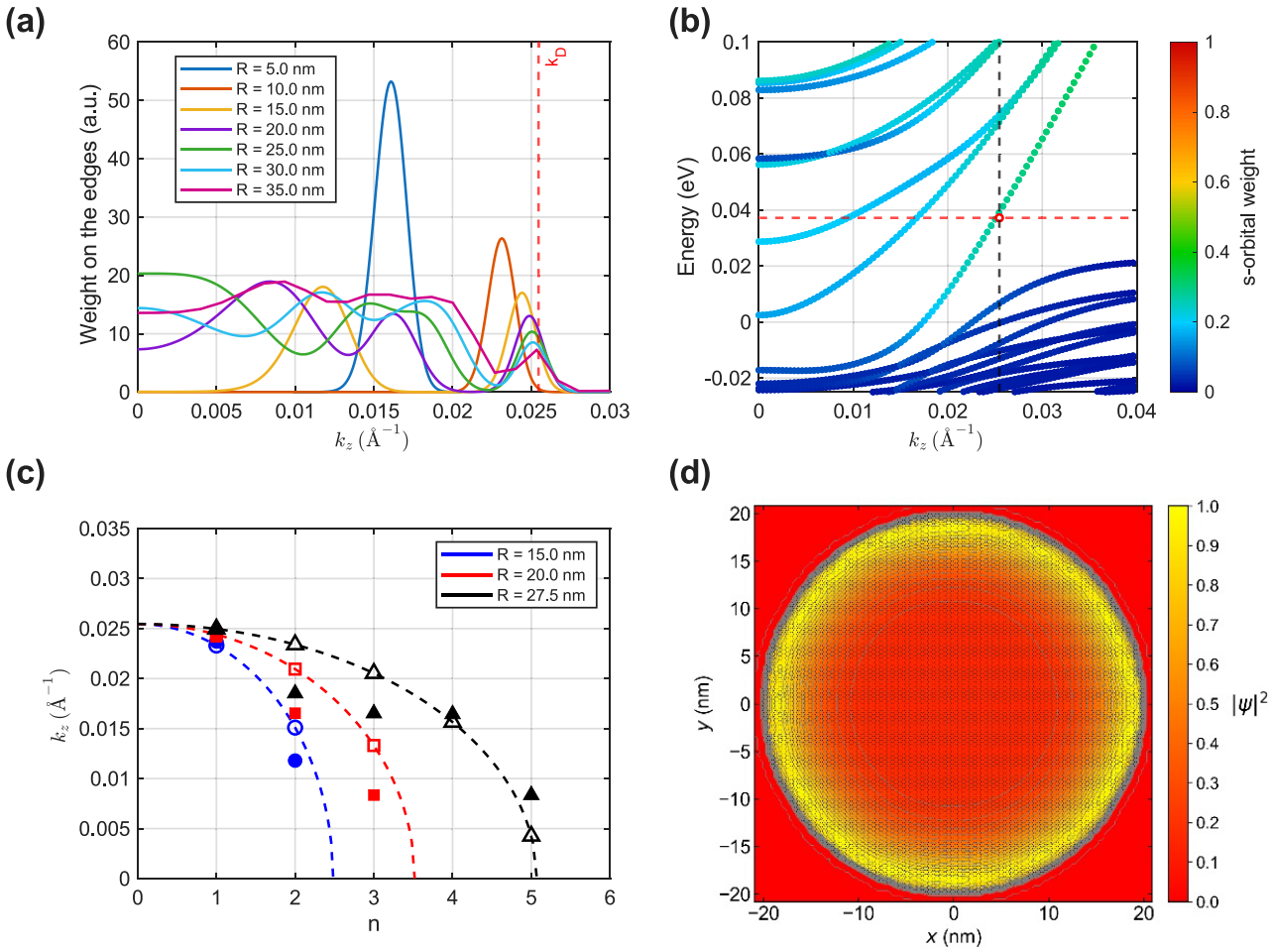


FIG. 5. Electronic properties and surface states of wz-HgTe nanowires. (a) LDOS on the nanowire edges at the energy of the Dirac point ($E_D = 37$ meV) illustrating the emergence of surface states with increasing radius $R$. For $R \to \infty$, these surface states tend to define a segment, analogous to Fermi-arc-like contours, connecting the points $k_z = \pm k_D$, projections of the Dirac points in the 1D Brillouin zone (the figure is symmetrical for $k_z < 0$). (b) Example of band structure for $R = 10$ nm, the color map indicating the $s$-orbital weight. The horizontal and vertical dashed lines indicate the energy $E_D$ and the position $k_D$ of a Dirac point projected in 1D. (c) The solid symbols (blue circles for $R = 15$ nm, red squares for 20 nm, and black triangles for 27.5 nm) represent the numerical values (calculated in TB) of $k_z$ for which the $n$th conduction band crosses the Dirac-point energy $E_D$. The hollow symbols correspond to the predictions from Eq. (10) with $\delta R = 3$ nm. The dashed lines serve as guides for the eyes. (d) Cross section in the $x$–$y$ plane of the wave function at energy $E = 0.029$ eV at $k_z = 0$ for $R = 10$ nm. The color map highlights the strong localization of the wave function at the edges of the nanowire.

contours that connect the projections of the two Dirac points within the 2D Brillouin zone [Fig. 4(b)].

Additional LDOS maps [Figs. 14(a)–14(e)] in Appendix E show a clear evolution of these surface states with film thickness. For the thinnest films (nevertheless thick enough to have a nonzero LDOS at the Dirac-point energy), Fermi-arc-like contours tend to split into two branches, except at two points close to the Dirac points (at $k_x = 0$). The gap between these doublets increases as the thickness decreases, reflecting the interaction between opposite surface states. Our analysis reveals that this interaction decreases exponentially with film thickness, with an estimated characteristic length of 6.3 nm [Fig. 14(f) of Appendix E]. As shown in Fig. 15 of Appendix E, the crossing of the two Fermi-arc-like contours at $k_x = 0$ evolves toward the bulk Dirac point $k_D$ within the Brillouin zone as the thickness increases. For sufficiently thick films, the Fermi-arc-like contours converge and are correctly described by the following equation:

$$(k_z/k_D)^2 + (k_x/k_M)^2 = 1, \tag{9}$$

with $k_M = 0.015$ Å$^{-1}$ for $(1\bar{1}00)$ thin films. We postulate that Fermi-arc-like contours persist in any thin film of wz-HgTe, provided that its growth axis is orthogonal to the crystallographic $c$ axis of the wurtzite structure. This hypothesis is supported by the results presented in Appendix E for $(11\bar{2}0)$ films. Although Eq. (9) remains applicable, the value of $k_M$ obtained for this orientation differs slightly from that previously reported (0.025 Å$^{-1}$).

### C. Discussion of the results

Taken together, these results highlight several important points. First, they show how the Dirac-semimetal phase recently established in bulk wz-HgTe [38] is reshaped by

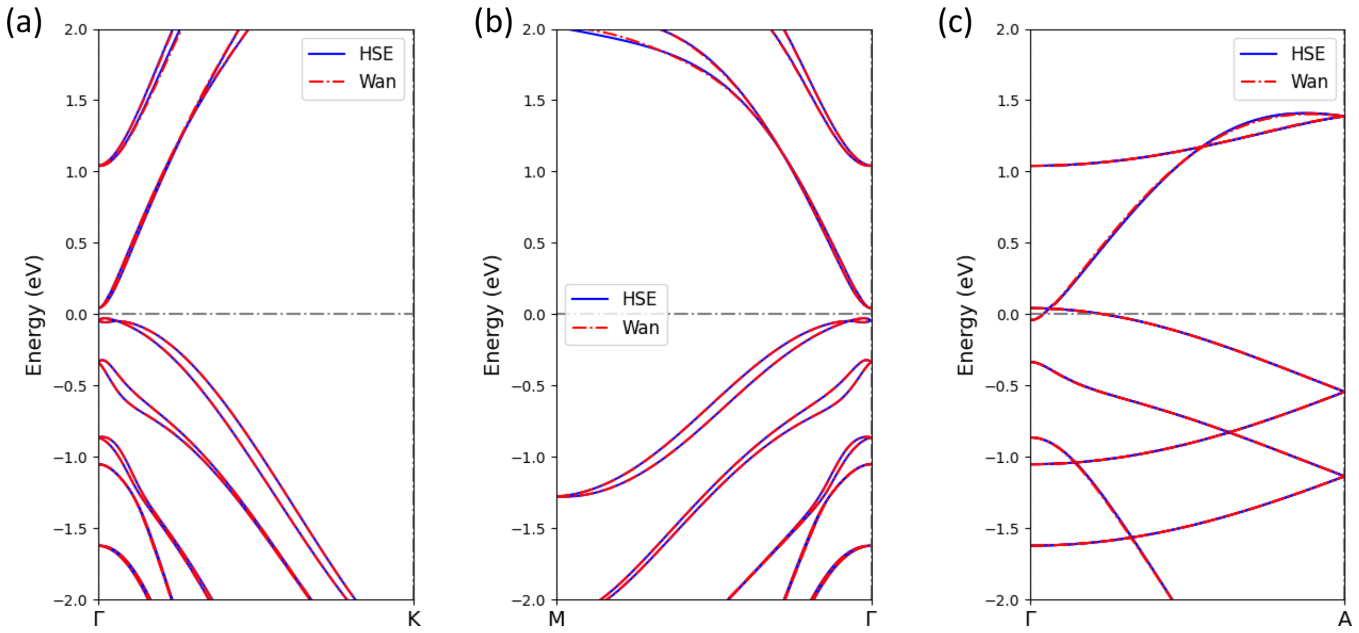


FIG. 6. Comparison of electronic structure computed from HSE and the Wannier model along (a) Γ–K, (b) M–Γ, and (c) Γ–A. Blue lines correspond to explicit zero-weight HSE band-path calculations; the Wannier model is used for interpolation.

reduced dimensionality and confinement. More specifically, they demonstrate that the topological response of wz-HgTe thin films depends strongly on the orientation of confinement with respect to the $c$ axis, and therefore on the way the bulk Dirac points are projected into the reduced Brillouin zone.

Second, our calculations reveal the presence of surface states at the Dirac-point energy in films whose growth axis is orthogonal to the $c$ axis, forming clearly identifiable Fermi-arc-like contours. Their emergence is not trivial. Indeed, Dirac points may be viewed as the superposition of two Weyl points of opposite chirality, but unlike in Weyl semimetals, the associated surface states are not generally protected by a topological invariant [31]. The observation of such Fermi-arc-like contours in wz-HgTe therefore shows that the absence of inversion symmetry does not preclude the formation of robust and well-defined surface features in experimentally relevant slab geometries.

More broadly, these results extend to noncentrosymmetric material platform phenomena that have so far been discussed mainly in centrosymmetric Dirac semimetals such as $Na_3Bi$ and $Cd_3As_2$. At the same time, they reveal a distinct physical situation: In wz-HgTe, the combination of inverted $s$–$p$ band ordering, crystal-field splitting, and inversion breaking produces an orientation-dependent topological behavior that goes beyond the standard centrosymmetric picture. Even if recent work has emphasized the fragility of Fermi-arc-like states in Dirac semimetals [57,58], our calculations show that they remain a useful and physically transparent description of the surface electronic structure in confined wz-HgTe.

## VI. ELECTRONIC STRUCTURE OF [001] wz-HgTe NANOWIRES

Finally, we consider nanowires along the $c$ axis as the one-dimensional confined limit of the same Dirac-point and surface-state physics. The results presented in the previous section suggest that wz-HgTe nanowires oriented along the $c$ crystallographic axis could also exhibit remarkable electronic properties. This relevance is reinforced by their structural similarity to nanorods synthesized by colloidal means [37]. In our previous study [38], we investigated nanowires with small diameters (<5 nm), in which the particularly pronounced quantum confinement effects lead to the opening of a significant energy gap, in agreement with experimental observations. In contrast, this work focuses on semimetallic nanowires with substantially larger diameters, with emerging surface states that arise from topological effects associated with Dirac points and which should be experimentally accessible. This contrasts with the previously studied strongly confined nanorods, for which the confinement energy dominates over the low-energy topological features of the bulk Dirac semimetal.

Figure 5(a) illustrates the LDOS calculated at the edges of wz-HgTe nanowires for different radii, at the Dirac-point energy $E_D$. We have found that the LDOS is comparatively negligible outside the interval $[-k_D, +k_D]$ of the Brillouin zone. For nanowires with small radii, this LDOS manifests itself in the form of discrete peaks (broadened by a Gaussian function with width $\sigma = 5$ meV), each corresponding to the intersection of a subband with the $E_D$ level [see Fig. 5(b)]. As the radius increases, the LDOS evolves toward a continuum connecting the projections of the two Dirac points. The localization at the edges is illustrated by a typical wave function of Fig. 5(d).

Figure 5(c) shows the values of $k_z$ at which the $n$th conduction subbands intersect $E_D$. Their number increases with the size of the nanowire. These results can be interpreted by considering the edge of a nanowire as a set of crystalline facets, all oriented perpendicular to the $c$ axis, an approximation that is all the more reasonable given that the nanowire is large. The edge states associated with these facets are then described by

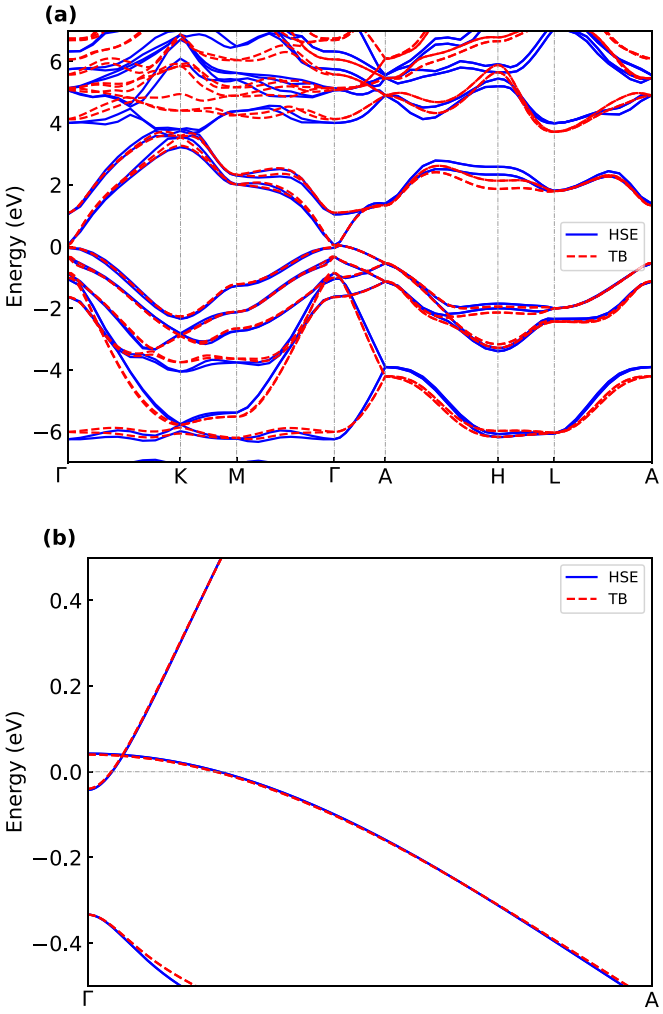


FIG. 7. (a) Band structure of wz-HgTe calculated using HSE (blue solid line) and TB (red dotted line). The zero of energy corresponds to the Fermi level. (b) Zoom in a low-energy region along the Γ–*A* direction. The Dirac point is at 37 meV above the Fermi level.

Fermi-arc-like contours, in accordance with Eq. (9). By imposing periodic boundary conditions along the circumference of the nanowire, we set the wavelength $\lambda = 2\pi(R - \delta R)/n$ (Bohr quantization condition), where $n$ is an integer. We can then replace $k_x$ by $2\pi/\lambda$ in Eq. (9), which gives

$$k_z = \pm k_D \sqrt{1 - \frac{1}{k_M^2}\left(\frac{n}{R - \delta R}\right)^2}, \tag{10}$$

in which $k_M = 0.0207$ is chosen as an average value between the $(1\bar{1}00)$ and $(11\bar{2}0)$ orientations. The parameter $\delta R$ reflects the penetration of the wave function into the volume of the nanowire, indicating that the states are not strictly confined to the surface. This very simple model, which leads to Eq. (10), explains rather well the position of the surface LDOS peaks collected in Fig. 5(c).

Our results suggest that the topological effects induced by the presence of Dirac points, intrinsic to the wurtzite structure, manifest themselves through the emergence of localized edge states in nanowires that are large enough to be semimetallic. These states could be demonstrated experimentally, in particular, by electronic transport measurements or scanning tunneling spectroscopy (STS) on large nanorods, the latter allowing their spatial location to be directly visualized.

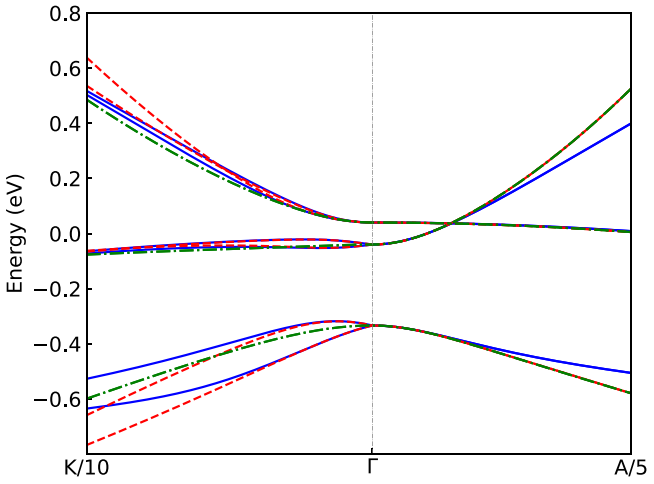


FIG. 8. TB (solid blue lines) and $\mathbf{k}\cdot\mathbf{p}$ (dashed red lines) band structures of bulk wz-HgTe along Γ–*K* and along Γ–*A*. The dash-dotted green lines represent the band structure obtained with $H_{12}(\mathbf{k}) = H_{21}(\mathbf{k}) = 0$.

## VII. CONCLUSION

The recent synthesis of HgTe nanostructures in the wurtzite phase [37,38] has opened access to a noncentrosymmetric material platform in which band inversion, crystal-field splitting, and reduced dimensionality can be explored on the same footing. Building on the recently established Dirac-semimetal character of bulk wz-HgTe, we have investigated how strain and quantum confinement reshape its topology beyond the strong-confinement regime explored so far.

By combining *ab initio*, tight-binding, and $\mathbf{k}\cdot\mathbf{p}$ approaches, we have shown that wz-HgTe exhibits a rich topological phase diagram governed by the interplay between the inverted *s*–*p* band ordering of HgTe and the crystal-field splitting specific to the wurtzite structure. In the bulk, biaxial strain drives a sequence of transitions from a Dirac semimetal to a three-dimensional topological insulator and eventually to a multiband metal. In confined geometries, the orientation relative to the *c* axis plays a central role: (0001) thin films undergo oscillatory transitions between trivial and topological insulating phases, whereas $(1\bar{1}00)$ films exhibit a single topological transition and, above a critical thickness, develop surface states with Fermi-arc-like character. In the same weak-confinement regime, semimetallic nanowires oriented along the *c* axis are predicted to host localized edge states. Taken together, the strain, thin-film, and nanowire results show that the topology of wz-HgTe is controlled by the fate of the bulk Γ–A Dirac points under band-order tuning, projection, and confinement.

Beyond the specific case of HgTe, these results show that noncentrosymmetric Dirac materials can display a topological response to strain and confinement that differs qualitatively from the more familiar centrosymmetric case. Wurtzite HgTe therefore appears not only as a confined infrared material in

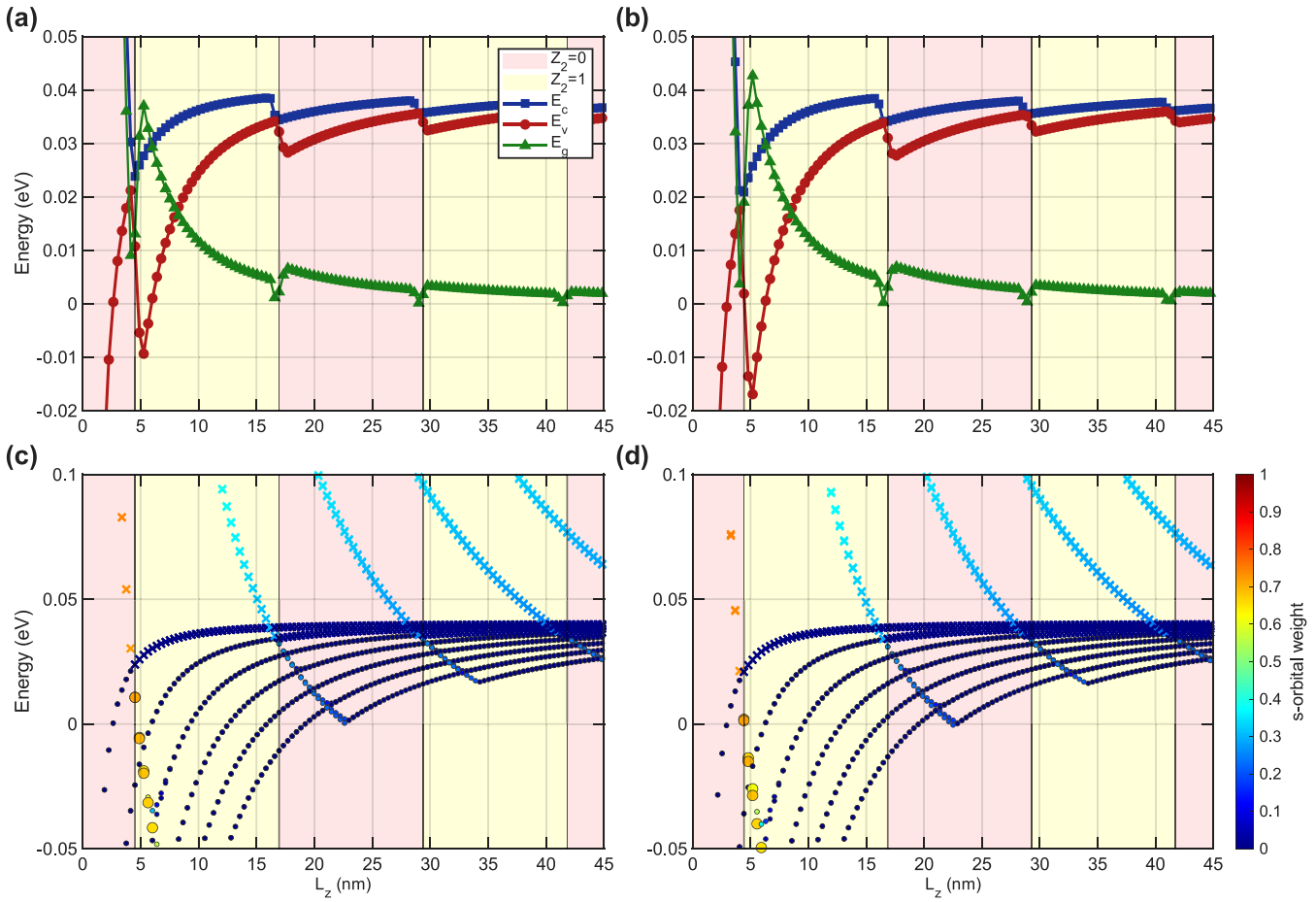


FIG. 9. Evolution of the energy band edges and band gap vs quantum well thickness for (a) Hg-Hg and (b) Hg-Te terminations. Panels (c) and (d) depict the electronic states near the Fermi level for Hg-Hg and Hg-Te terminations, respectively, highlighting the *s*-orbital weight. The background colors denote the topological phase: trivial (pink, $Z_2 = 0$) and topological (yellow, $Z_2 = 1$).

the strong-confinement regime [38], but also as a promising host for strain-tunable and orientation-dependent topological phases when the confinement is reduced. This perspective calls for experimental studies of thicker films, nanoplatelets, and larger nanowires with controlled orientation, as well as for further theoretical work on the robustness of the predicted surface and edge states against perturbations, disorder, and realistic electrostatic environments.

## ACKNOWLEDGMENTS

This work was supported by the French National Research Agency (ANR Project QuickTera No. ANR-22-CE09-0018). Part of the calculations were performed using computational resources provided by GENCI-IDRIS (Grant No. 2026-A0190912036). We are grateful to Emmanuel Lhuillier for valuable discussions during the preparation of this manuscript.

## DATA AVAILABILITY

The data that support the findings of this article are not publicly available. The data are available from the authors upon reasonable request.

## APPENDIX A: WANNIER MODEL

The Dirac-point position was not determined from the $6 \times 6 \times 4$ self-consistent $k$-mesh. Instead, explicit zero-weight HSE $k$-points were used along the high-symmetry paths shown in Fig. 6. The resulting HSE bands were used to construct and validate the Wannier Hamiltonian. After this validation, the Wannier model was used as an interpolation tool to sample the Γ–A direction more densely and determine $k_D$. The purpose of this comparison is not to reestablish the bulk Dirac-semimetal phase, already reported in Ref. [38], but to validate the Wannier model used here for interpolation and for the subsequent analysis of strain and confinement effects.

## APPENDIX B: TIGHT-BINDING PARAMETERS FOR wz-HgTe

The TB parameters are given in Table II. The zero of energy corresponds to the Fermi level determined in HSE. The terms $E$ represent the on-site matrix elements, $E_s$ being, for example, the $s$ orbital energy in the solid. The energy of the $p_z$ orbitals is not the same as that of the $p_x$ and $p_y$ orbitals, because the wurtzite structure is asymmetrical. For simplicity, we assume that the energies of the $d$ orbitals are all identical. Note that these $d$ orbitals are used to describe

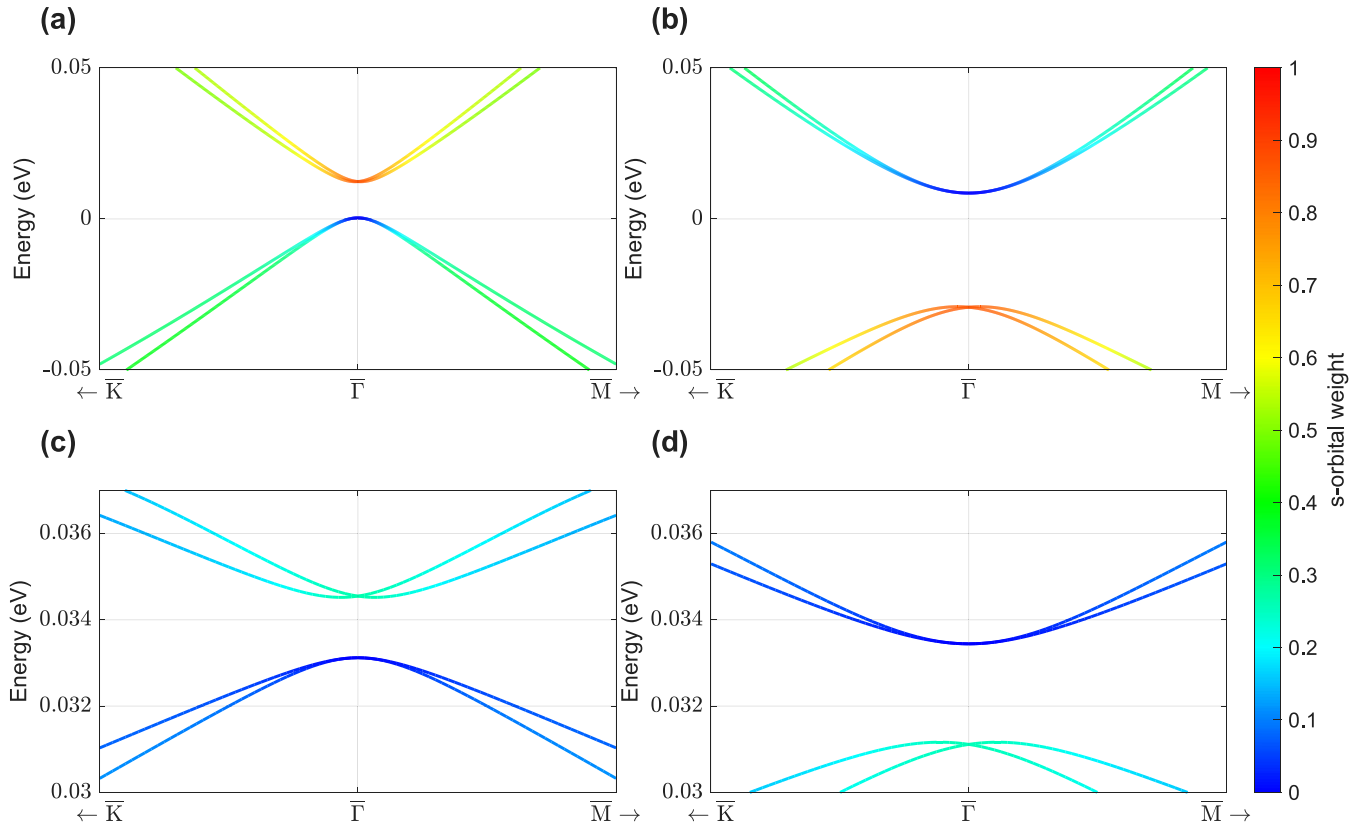


FIG. 10. Electronic band structures of (0001) films of wz-HgTe with Te-Te termination across topological phase transitions (film thicknesses are given in Table I). Panels (a) and (b) illustrate the first transition from a trivial to a topological-insulator phase. Panels (c) and (d) depict the second transition from a topological back to a trivial phase. The color map indicates the *s*-orbital weight, highlighting the orbital character transfer between the conduction and valence bands at each critical thickness.

the conduction bands, not the filled rather flat Hg 5*d* bands between −7 and −10 eV obtained using the HSE calculations. The terms $V$ in Table II define the hopping matrix elements in the two-center approximation as shown by Slater and Koster [59]. For example, $V_{sp\sigma}$(ac) represents the ($sp\sigma$) hopping term between an *s* orbital on a Te atom and a *p* orbital on a neighbor Hg atom, the *p* orbital pointing along the axis between the two atoms, following the notations of Ref. [59].

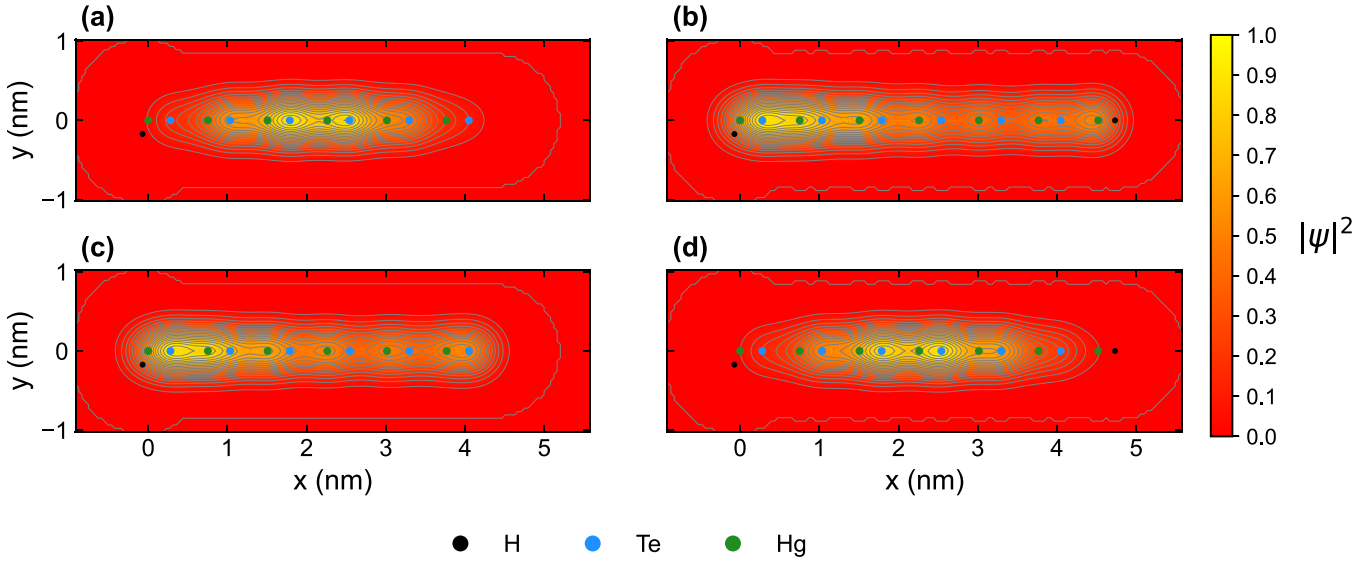


FIG. 11. Calculated wave functions at the Γ point for the highest valence band and lowest conduction band before and after the topological transition. Panels (a) and (c) show the valence band and lowest conduction band states, respectively, in the trivial phase. Panels (b) and (d) show the corresponding states after the transition.

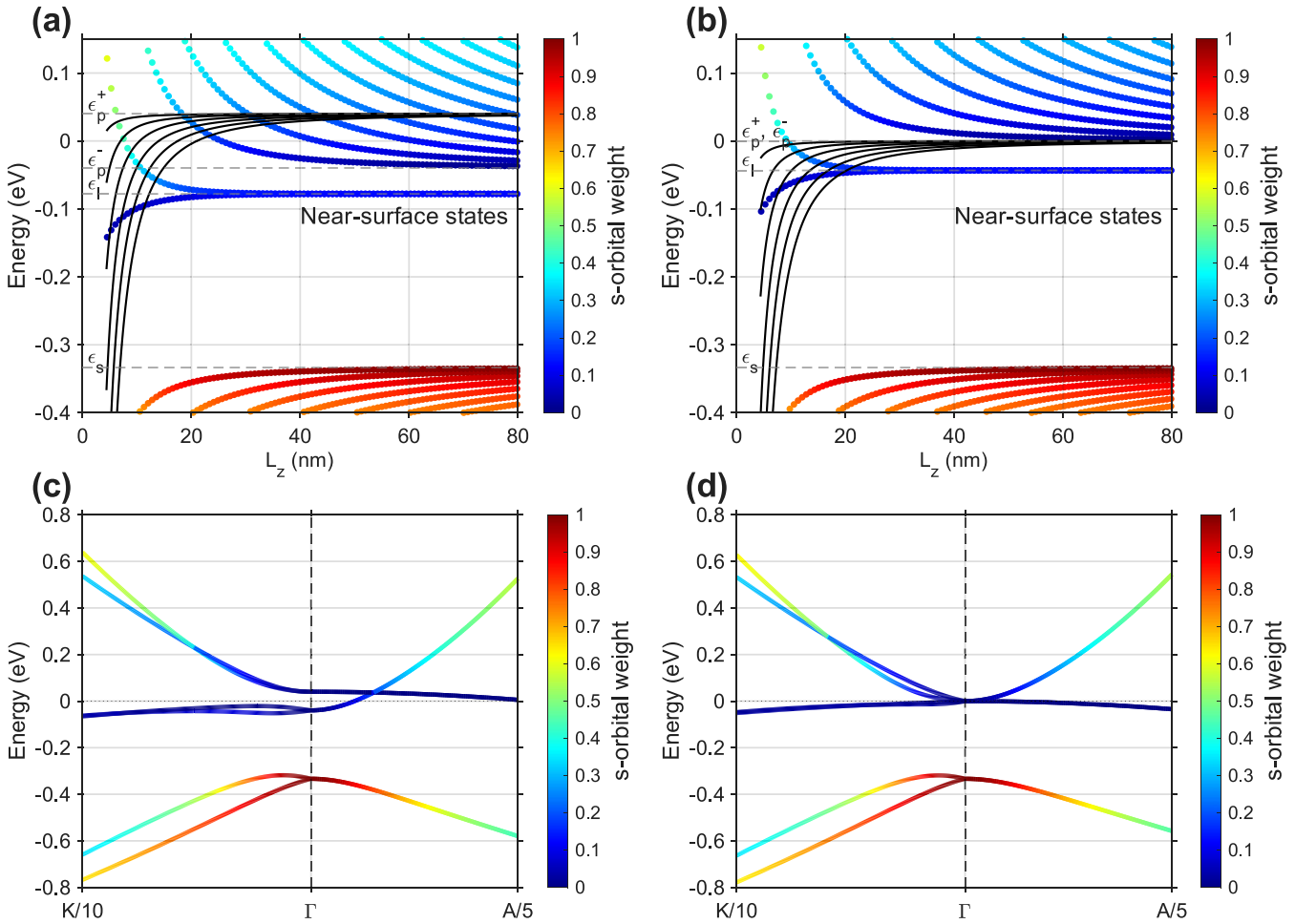


FIG. 12. (a) Electronic energy levels at $k_x = k_y = 0$ as a function of the quantum well thickness $L_z$ within the $6 \times 6$ $\mathbf{k} \cdot \mathbf{p}$ model. The solid lines represent purely $p$ states with an energy dispersion $E_0(k_n)$, where $k_n = n\pi/L_z$ ($n = 1, \ldots, 6$). (b) Same as panel (a) but with $\varepsilon_p^+ = \varepsilon_p^- = 0$, simulating the absence of crystal-field splitting. (c) Calculated $6 \times 6$ $\mathbf{k} \cdot \mathbf{p}$ band structure using the parameters from panel (a). (d) Band structure using the parameters from panel (b), showcasing the absence of Dirac points.

For a nonideal wurtzite structure of lattice parameters $a$ and $c$, and internal lattice parameter $u \neq 3/8$, it must be taken into account that not all interatomic distances between neighboring atoms are equivalent. The bonds oriented along $c$ have a different length $d_0 = uc$ than the other bonds, $d = \sqrt{3c^2(1-2u)^2 + 4a^2}/(2\sqrt{3})$. Following the approach described in Ref. [60], we therefore write the hopping term between two orbitals $\alpha$ and $\beta$ on nearest neighbors at distance $d$ as

$$V_{\alpha\beta}(d) = V_{\alpha\beta}(d_0)\left(\frac{d_0}{d}\right)^{\eta_{\alpha\beta}}, \tag{B1}$$

where the hopping term $V_{\alpha\beta}(d_0)$ at distance $d_0$ and the exponent $\eta_{\alpha\beta}$ are given in Table II.

In the case of HgTe QDs, pseudohydrogen atoms are used to passivate their surface [51,52]. The Hg-H and Te-H parameters are defined in order to push the surface states far from the band edges.

Figure 7 illustrates remarkable agreement between the HSE calculations and the TB model over a wide range of energies and across the entire Brillouin zone. This agreement persists near the Γ point, particularly in the vicinity of the Dirac points.

## APPENDIX C: DERIVATION OF A k · p MODEL FROM TIGHT-BINDING CALCULATIONS

We present the method used to derive the $\mathbf{k} \cdot \mathbf{p}$ matrix directly from TB calculations for the bulk. The TB Hamiltonian $H$ is written in the basis of Bloch functions as a function of $\mathbf{k}$. $H$ is diagonalized at $\mathbf{k} = 0$. The eigenvectors form a complete basis of the system. Third, we write $H$ in this basis up to the second order in $\mathbf{k}$,

$$H = H^{(0)} + H^{(1)} + H^{(2)}, \quad H^{(1)} = \sum_{i=x,y,z}\left(\frac{dH}{dk_i}\right)k_i,$$
$$H^{(2)} = \frac{1}{2}\sum_{i,j=x,y,z}\left(\frac{d^2H}{dk_i dk_j}\right)k_i k_j, \tag{C1}$$

in which the derivatives are calculated numerically at $\mathbf{k} = 0$.

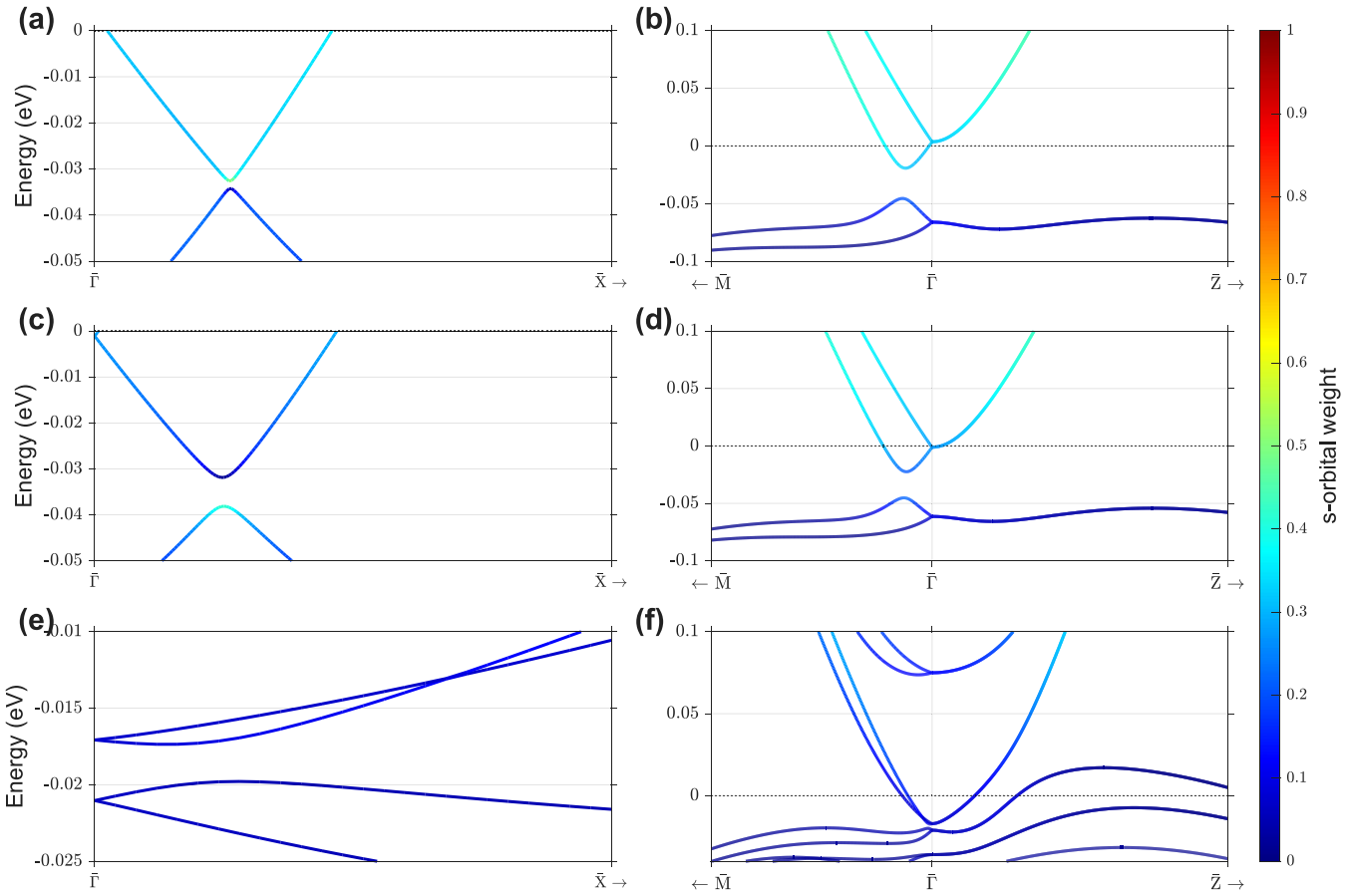


FIG. 13. Electronic band structures of thin $(1\bar{1}00)$ wz-HgTe films. Panels (a) and (b) show the near-Fermi level states for a 4.5 nm film in the trivial phase ($Z_2 = 0$) along the $\bar{\Gamma}$–$\bar{X}$ and $\bar{M}$–$\bar{\Gamma}$–$\bar{Z}$ paths, respectively. Panels (c) and (d) depict the 4.9 nm film immediately following the topological transition ($Z_2 = 1$). Panels (e) and (f) illustrate the band structure for a 19.4 nm film, highlighting the persistence of a gap at each $k$ point, despite the negative global gap (semimetalic character).

We define the subset of the basis in which the $\mathbf{k}\cdot\mathbf{p}$ model will be defined, i.e., in the present case, the lowest conduction states and the two highest valence states (all twofold degenerate). We use the Luttinger-Kohn theory of perturbation [61]. If we write $H$ as $\mathcal{H} + V$, where $\mathcal{H}$ contains just the terms restricted to the subspace and $V$ the others, the renormalized Hamiltonian $\tilde{H}$ in the subspace is given to the second order in $V$ by

$$\tilde{H}_{IJ} = \mathcal{H}_{IJ} + \frac{1}{2}\sum_n V_{In}V_{nJ}\left(\frac{1}{E_{In}} + \frac{1}{E_{Jn}}\right), \tag{C2}$$

in which we represent the states of the subspace by uppercase letters, e.g., $I$ of energy $E_I$, and the other states of the basis by lowercase ones, e.g., $n$ of energy $E_n$. If we use for $H$ its expression given in Eq. (C1), the $\mathbf{k}\cdot\mathbf{p}$ Hamiltonian restricted to second-order terms in $\mathbf{k}$ is given by

$$\tilde{H}_{IJ} = H^{(0)}_{IJ} + H^{(1)}_{IJ} + H^{(2)}_{IJ} + \frac{1}{2}\sum_n H^{(1)}_{In}H^{(1)}_{nJ}\left(\frac{1}{E_{In}} + \frac{1}{E_{Jn}}\right). \tag{C3}$$

This allows to completely define the $\mathbf{k}\cdot\mathbf{p}$ Hamiltonian, without adjustable parameters. The last term of Eq. (C3) describes the effect of remote bands that lead to a renormalization of the $\mathbf{k}\cdot\mathbf{p}$ parameters.

As described in Sec. II C, we derived a $6\times 6$ Hamiltonian whose parameters are $\varepsilon_p^+ = 40.2$ meV, $\varepsilon_p^- = -39.7$ meV, $\varepsilon_s = -333.5$ meV, $C_0^{\parallel} = 5.64626$ eV Å$^2$ and $C_0^z = 13.682\,09$ eV Å$^2$, $D_p^+ = 14.495\,86$ eV Å$^2$, $C_p^+ = 18.671\,06$ eV Å$^2$, $D_p^- = 9.950\,55$ eV Å$^2$, $C_p^- = 21.762\,34$ eVÅ$^2$, $D_s = 24.446\,41$ eV Å$^2$, $C_s = 40.433\,41$ eV Å$^2$, $A = 6.57$ eV Å, $P = 1.179\,78$ eV Å, $Q = 5.765\,99$ eV Å, $R = 1.445\,25$ eV Å, $S = 3.321\,57$ eV Å, and $T = 2.604\,80$ eV Å. Derived parameters used in the main text are $M = C_p^- - C_0^z$, $N = C_0^z + C_s$, and $L = C_p^+ - C_0^z$. Note that we have neglected the very small nondiagonal quadratic terms of $H(\mathbf{k})$.

Figure 8 shows that the $\mathbf{k}\cdot\mathbf{p}$ Hamiltonian gives a fairly good representation of the band structure not only in the vicinity of $k = 0$ but also around the Dirac point.

## APPENDIX D: ADDITIONAL RESULTS ON (0001) FILMS

### 1. Influence of surface terminations

Figures 9(a) and 9(b) illustrate the evolution of the energy band edges ($E_v$ and $E_c$) and the band gap ($E_g$) as a

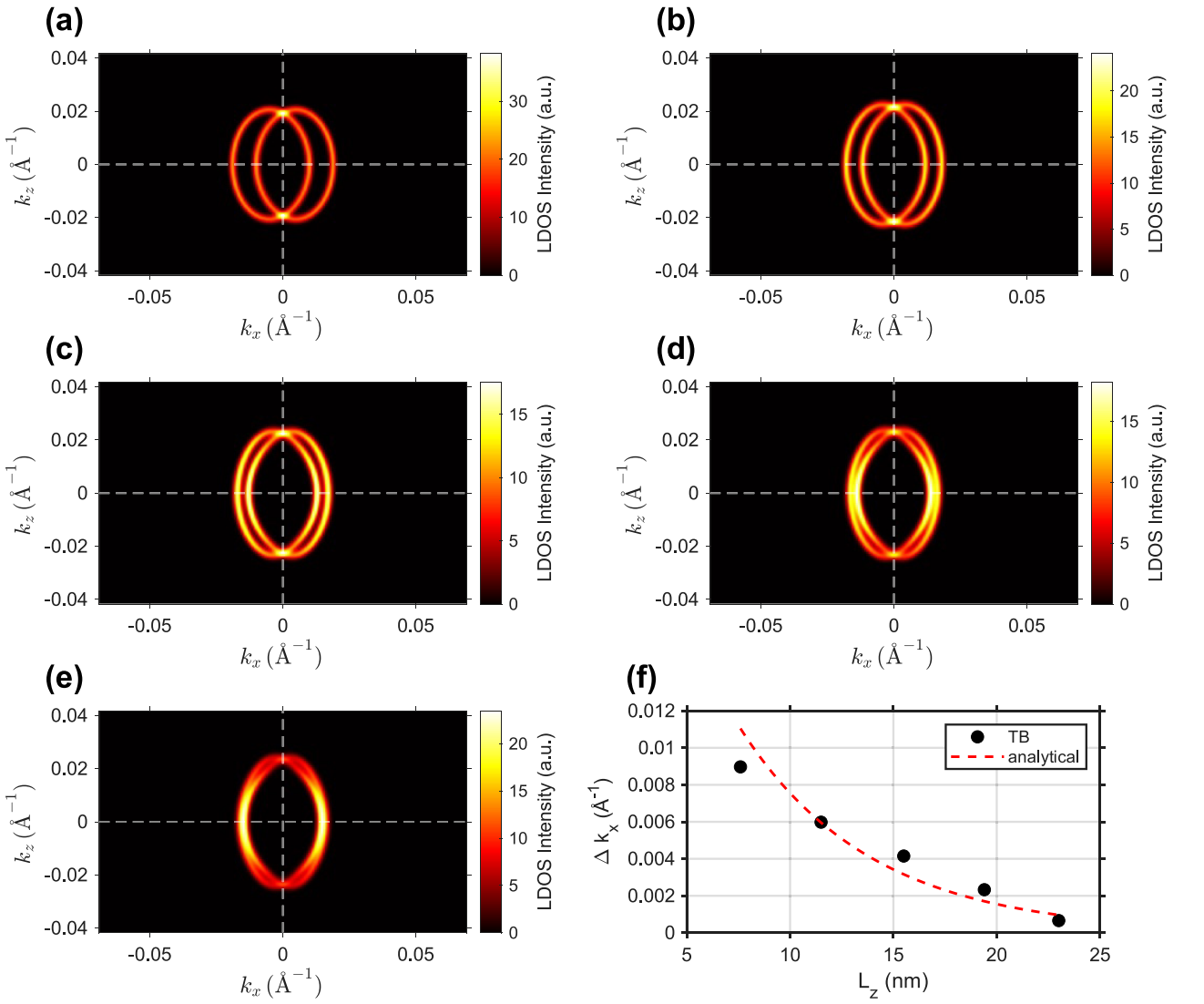


FIG. 14. Evolution of the surface LDOS displaying Fermi-arc-like contours in $(1\bar{1}00)$ films for varying thicknesses: (a) 7.6 nm, (b) 11.5 nm, (c) 15.5 nm, (d) 19.4 nm, and (e) 23.0 nm. (f) Separation $\Delta k_x$ between the two split Fermi-arc-like contours at $k_z = 0$ as a function of the film thickness $L_z$. The dashed red line represents an analytical fit using an exponential decay model $\Delta k_x = A \exp(-L_z/L_0)$, with $A = 0.0368$ Å$^{-1}$ and a penetration depth $L_0 = 63.16$ Å.

function of the film thickness for Hg-Hg and Hg-Te terminations, respectively. Additionally, Figs. 9(c) and 9(d) depict the electronic states near the Fermi level for these same configurations.

Consistent with the case of Te-Te termination discussed in the main text, the system exhibits periodic oscillations in its topological nature, as seen in Fig. 9. For the Hg-Hg termination, the system undergoes four successive topological transitions at critical thicknesses of 4.15 nm (trivial to topological), 16.58 nm (topological to trivial), 29.01 nm (trivial to topological), and 41.44 nm (topological to trivial). Similarly, four transitions are observed for the Hg-Te termination at 4.05, 16.48, 28.91, and 41.35 nm, following the same sequence of phase inversions. It is noteworthy that these topological transitions occur at thicknesses slightly larger than those obtained for the Te-Te terminations previously discussed, which shows the importance of the edges. However, the relative difference is mainly important for the first topological transition involving the near-surface state.

### 2. Band structures at topological transitions

Figures 10(a) and 10(b) illustrate the primary transition from a trivial to a topological-insulator phase in a (0001) film of wz-HgTe with Te-Te termination. This quantum phase change is characterized by a significant shift in the *s*-orbital character; a high *s*-orbital weight (approximately 0.8) is observed in the conduction band prior to the transition, which subsequently transfers to the valence band upon reaching the topological phase. This inversion originates from a $\Gamma_6$–$\Gamma_8$ band inversion, similar to the topological transition in zb-HgTe [35].

In contrast, Figs. 10(c) and 10(d) display the second transition, where the system reverts from a topological to a trivial insulator. While this also involves a transfer of *s*-orbital

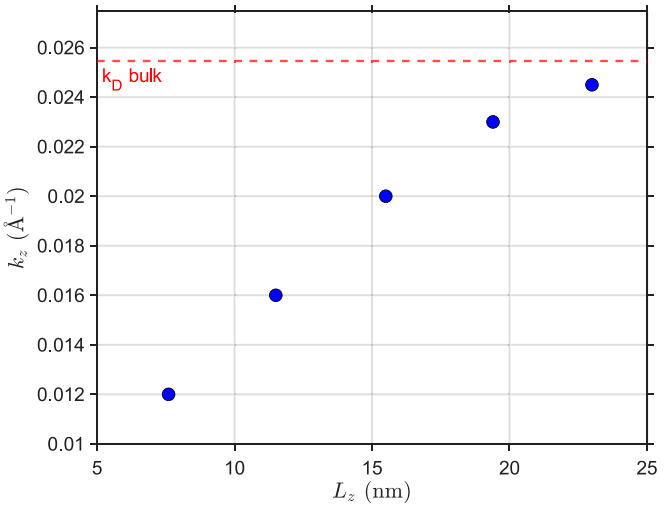


FIG. 15. Evolution of the Fermi arc crossing point $k_z$ (evaluated at $k_x = 0$) as a function of the film thickness $L_z$. The red dashed line represents the wave vector $k_D$ of the bulk Dirac point in wz-HgTe.

weight from the conduction to the valence band, the magnitude of the weight is notably lower (around 0.2) due to a different physical origin compared to the first transition. Specifically, this second transition and the subsequent ones discussed in the main text arise from the Dirac points located along the $\Gamma$–$A$ path in the bulk Brillouin zone. They arise from the crossover between purely $p$ states and states with a small $s$ component, the latter decreasing as the thickness increases.

### 3. Wave functions

Before the topological transition, the highest valence state [Fig. 11(a)] is localized at the center of the film, while the lowest conduction state [Fig. 11(c)] is localized at the edges. Beyond the transition, an inversion occurs: The two states exchange their respective localizations. For the reasons discussed in the main text, we do not find those near-surface states for successive topological transitions.

### 4. Application of the k · p model to (0001) films

The most efficient approach to solving the $\mathbf{k}\cdot\mathbf{p}$ equations for (0001) layers is to consider that the $2\times 2$ block of Eq. (8) is the second-order expansion of an effective $2\times 2$ TB Hamiltonian. To do this, we consider a 1D crystal with lattice parameter $a$ along $z$, where each site $i$ of position $ia$ is characterized by an $s$ orbital $|s_i\rangle$ and a $p_z$ orbital $|p_i\rangle$. The hopping terms are restricted to the nearest neighbors. Writing $E_s = \langle s_i|H|s_i\rangle$, $E_p = \langle p_i|H|p_i\rangle$, $\beta_{ss} = \langle s_i|H|s_{i+1}\rangle$, and $\beta_{sp} = \langle s_i|H|p_{i+1}\rangle$, $\beta_{pp} = \langle p_i|H|p_{i+1}\rangle$, the TB Hamiltonian in the basis of Bloch functions $\sum_i \exp(ik_z a)|s_i\rangle$ and $\sum_i \exp(ik_z a)|p_i\rangle$ is given by

$$\begin{pmatrix} E_s + 2\beta_{ss}\cos(k_z a) & 2i\beta_{sp}\sin(k_z a) \\ -2i\beta_{sp}\sin(k_z a) & E_p + 2\beta_{pp}\cos(k_z a) \end{pmatrix}. \tag{D1}$$

TABLE II. TB parameters (notations of Slater and Koster [59]) for wz-HgTe in an orthogonal $sp^3d^5s^*$ model. $\Delta$ is the spin-orbit coupling. (a) and (c) denote the anion (Te) and the cation (Hg), respectively. Lattice parameters: $a = 4.546$ Å and $c = 7.535$ Å. Internal lattice parameter: $u = 0.371852$. The hopping terms $V$ are given for the interatomic distance $d_0 = uc$.

| Parameters for wz-HgTe (eV) | | | |
|---|---|---|---|
| $E_s$(a) | −10.126 081 | $E_s$(c) | −1.588 744 |
| $E_{p_x}$(a) | 1.538 488 | $E_{p_x}$(c) | 6.234 048 |
| $E_{p_y}$(a) | 1.538 488 | $E_{p_y}$(c) | 6.234 048 |
| $E_{p_z}$(a) | 1.611 872 | $E_{p_z}$(c) | 5.690 216 |
| $E_d$(a) | 12.005 981 | $E_d$(c) | 14.472 114 |
| $E_{s^*}$(a) | 17.021 550 | $E_{s^*}$(c) | 11.809 551 |
| $\Delta$(a) | 0.284 773 | $\Delta$(c) | 0.439 924 |
| $V_{ss\sigma}$(ac) | −0.920 309 | $V_{s^*s^*\sigma}$(ac) | −1.541 776 |
| $V_{ss^*\sigma}$(ac) | 0.344 932 | $V_{ss^*\sigma}$(ca) | −0.245 447 |
| $V_{sp\sigma}$(ac) | 1.017 994 | $V_{sp\sigma}$(ca) | 2.287 185 |
| $V_{ps^*\sigma}$(ac) | −1.613 963 | $V_{ps^*\sigma}$(ca) | −1.109 925 |
| $V_{sd\sigma}$(ac) | −0.497 824 | $V_{sd\sigma}$(ca) | −1.126 995 |
| $V_{ds^*\sigma}$(ac) | 0.659 815 | $V_{ds^*\sigma}$(ca) | 0.453 121 |
| $V_{pp\sigma}$(ac) | 3.464 790 | $V_{pp\pi}$(ac) | −1.047 079 |
| $V_{pd\sigma}$(ac) | −1.662 395 | $V_{pd\sigma}$(ca) | −0.624 430 |
| $V_{pd\pi}$(ac) | 1.333 669 | $V_{pd\pi}$(ca) | 1.732 023 |
| $V_{dd\sigma}$(ac) | −0.511 953 | $V_{dd\pi}$(ac) | 2.667 644 |
| $V_{dd\delta}$ | −1.112 231 | | |
| $\eta_{ss\sigma}$(ac) | 3.5 | $\eta_{s^*s^*\sigma}$(ac) | 0.0 |
| $\eta_{ss^*\sigma}$(ac) | 2.0 | $\eta_{ss^*\sigma}$(ca) | 2.0 |
| $\eta_{sp\sigma}$(ac) | 5.0 | $\eta_{sp\sigma}$(ca) | 5.0 |
| $\eta_{ps^*\sigma}$(ac) | 1.0 | $\eta_{ps^*\sigma}$(ca) | 1.0 |
| $\eta_{sd\sigma}$(ac) | 1.0 | $\eta_{sd\sigma}$(ca) | 1.0 |
| $\eta_{ds^*\sigma}$(ac) | 4.0 | $\eta_{ds^*\sigma}$(ca) | 4.0 |
| $\eta_{pp\sigma}$(ac) | 4.0 | $\eta_{pp\pi}$(ac) | 3.5 |
| $\eta_{pd\sigma}$(ac) | 1.0 | $\eta_{pd\sigma}$(ca) | 1.0 |
| $\eta_{pd\pi}$(ac) | 1.0 | $\eta_{pd\pi}$(ca) | 1.0 |
| $\eta_{dd\sigma}$(ac) | 2.0 | $\eta_{dd\pi}$(ac) | 2.0 |
| $\eta_{dd\delta}$ | 2.0 | | |
| Parameters for Hg-H and Te-H (eV) | | | |
| $E_H$ | 2.746 38 | | |
| $V_{ss\sigma}$ | −35.697 27 | $V_{sp\sigma}$ | 61.829 48 |

By comparing its expression in the second order in $k_z$ with Eq. (8), we obtain

$$\beta_{sp} = \frac{A}{2a},\ \beta_{ss} = -\frac{N}{a^2},\ E_s = \varepsilon_s + 2\frac{N}{a^2},\ \beta_{pp} = \frac{M}{a^2},$$
$$E_p = \varepsilon_p^- - 2\frac{M}{a^2}. \tag{D2}$$

The electronic structure of thin films is simply obtained by diagonalizing the effective model Hamiltonian for a finite linear chain.

### 5. Analytical expression of near-surface states

The $\mathbf{k}\cdot\mathbf{p}$ model allows near-surface states to be determined analytically. We assume a semi-infinite wz-HgTe substrate (bounded by $z < 0$), where the state is written as $F(z)|u_p^-\rangle + G(z)|u_s\rangle$, $|u_p^-\rangle$ and $|u_s\rangle$ being the Bloch functions at $\Gamma$ of energy $\varepsilon_p^-$ and $\varepsilon_s$, respectively. From the $2\times 2$ block of Eq. (8),

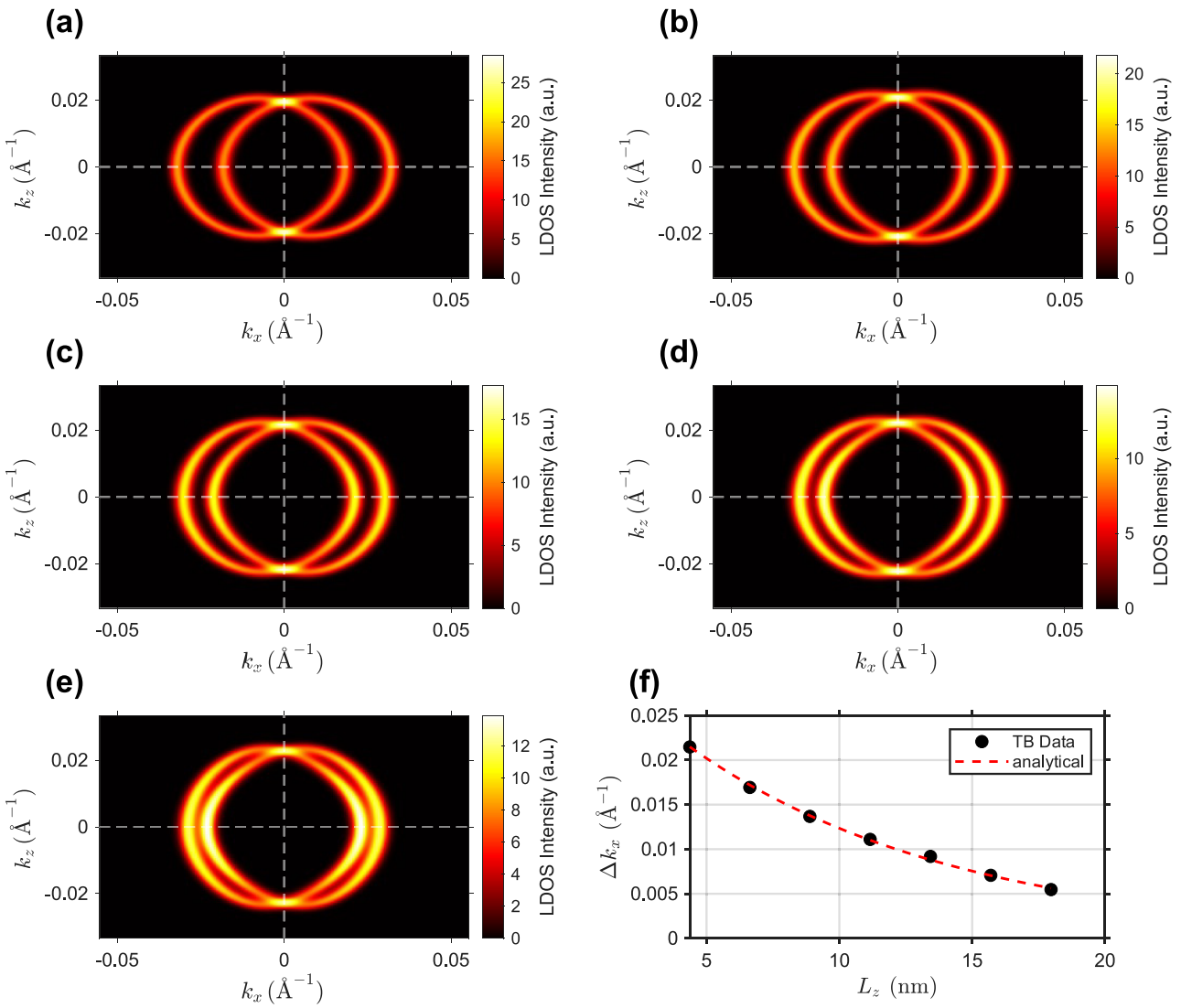


FIG. 16. Evolution of the surface LDOS displaying Fermi-arc-like contours in $(11\bar{2}0)$ films for varying thicknesses: (a) 8.9 nm, (b) 11.2 nm, (c) 13.4 nm, (d) 15.7 nm, and (e) 18.0 nm. (f) Separation $\Delta k_x$ between the two split Fermi-arc-like contours at $k_z = 0$ as a function of the film thickness $L_z$. The dashed red line represents an analytical fit using an exponential decay model $\Delta k_x = A\exp(-L_z/L_0)$, with $A = 0.033$ Å$^{-1}$ and a penetration depth $L_0 = 10.16$ Å.

$F$ and $G$ are solutions of the following differential equations:

$$(\varepsilon_p^- - E)F(z) + M\frac{\partial^2 F(z)}{\partial z^2} - A\frac{\partial G(z)}{\partial z} = 0,$$
$$A\frac{\partial F(z)}{\partial z} + (\varepsilon_s - E)G(z) - N\frac{\partial^2 G(z)}{\partial z^2} = 0. \quad \text{(D3)}$$

Seeking solutions of the form $F(z) = F^0\exp(\alpha z)$ and $G(z) = G^0\exp(\alpha z)$ such that $F(0) = G(0) = 0$, we obtain a single solution in the interval $[\varepsilon_s, \varepsilon_p^-]$ for $E = \varepsilon_I = (M\varepsilon_s + N\varepsilon_p^-)/(M+N)$ such that $G(z) = \sqrt{(M/N)}F(z)$ and

$$F(z) = F_0(\exp(\alpha^- z) - \exp(\alpha^+ z)), \quad \text{(D4)}$$

$$\alpha^{\pm} = \frac{A}{2\sqrt{MN}} \pm \frac{1}{2}\sqrt{\frac{A^2}{MN} - 4k_I^2}, \quad \text{(D5)}$$

with $k_I^2 = (\varepsilon_p^- - \varepsilon_s)/(M+N)$.

#### 6. 6 × 6 k · p model in the absence of crystal-field splitting

To shed further light on the physical origin of the periodic topological transitions, we can manipulate the parameters of the **k** · **p** Hamiltonian. Panels (a) and (c) of Fig. 12 are obtained using the diagonal energy parameters: $\varepsilon_p^+ = 0.040\,17$, $\varepsilon_p^- = -0.039\,71$, and $\varepsilon_s = -0.333\,48$. These values explicitly account for the crystal-field splitting inherent to the wurtzite structure. In contrast, panels (b) and (d) depict the system in a configuration where $\varepsilon_p^+ = \varepsilon_p^- = 0$. By neglecting the crystal-field splitting, this configuration qualitatively simulates zb-HgTe-like behavior. The band structure in Fig. 12(d) shows the disappearance of the Dirac points. Under these conditions, we observe that the valence states no longer cross the conduction states as a function of $L_z$ [Fig. 12(b)]. This confirms that the observed oscillations in the topological nature of the system stem directly from the specific symmetries of the wurtzite lattice, which gives rise to a Dirac point along

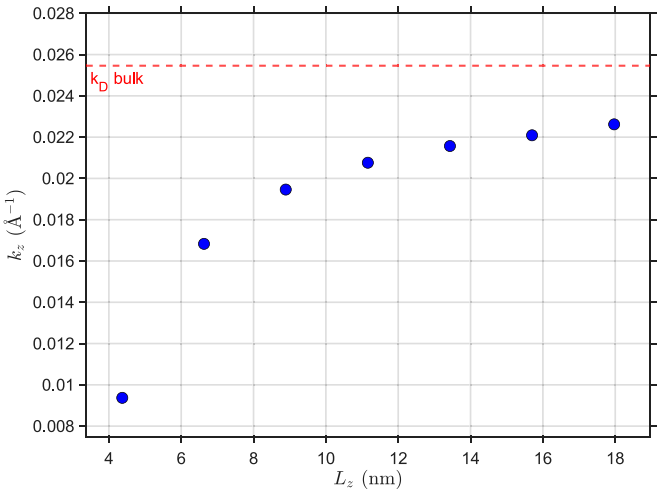


FIG. 17. Evolution of the Fermi arc crossing point $k_z$ (evaluated at $k_x = 0$) in $(11\bar{2}0)$ films as a function of the film thickness $L_z$. The red dashed line represents the wave vector $k_D$ of the bulk Dirac point in wz-HgTe.

the $\Gamma$–$A$ path, ultimately driving the higher-order topological transitions.

## APPENDIX E: ADDITIONAL RESULTS ON $(1\bar{1}00)$ FILMS

### 1. Band structures

Figure 13 illustrates the electronic band structures of $(1\bar{1}00)$ films before and after the first topological phase transition. For this orientation, the transition is uniquely driven by the $s$–$p$ band inversion. While this behavior is qualitatively similar to that observed in (0001) films, the $s$-orbital weight is notably less pronounced in the $(1\bar{1}00)$ geometry.

As discussed in the main text, this system exhibits a single topological transition. As demonstrated in Fig. 13(e), a finite energy gap is preserved at each $k$ point, even for the thickness of 19.4 nm. A similar gap remains present along the $\bar{M}$–$\bar{\Gamma}$ and $\bar{\Gamma}$–$\bar{Z}$ directions [Fig. 13(f)]. However, for $L_z = 19.4$ nm, the film is semimetallic, and the valence and conduction bands overlap energetically.

The $\bar{\Gamma}$–$\bar{Z}$ direction in the film Brillouin zone corresponds to the $\Gamma$–$A$ path in the bulk limit. The upward dispersion of the valence states toward the conduction bands along this specific path is a direct signature of the Dirac-point formation characteristic of the bulk wz-HgTe phase.

### 2. Fermi-arc-like contours in $(1\bar{1}00)$ films

In Fig. 14, we illustrate the evolution of the Fermi-arc-like contours obtained by calculating the surface LDOS. To isolate the surface contributions, the LDOS is defined as

$$\mathrm{LDOS}(E, \mathbf{k}) = \sum_j |\psi_j(\mathbf{k})|^2 \delta(E - E_j(\mathbf{k})), \qquad \text{(E1)}$$

where $E_j(\mathbf{k})$ is the eigenenergy of the system, and the sum runs over all relevant eigenstates, the spatial projection onto the edge atomic sites, and the spin components. The LDOS is strictly restricted to the surface states by considering only the atoms located within a depth of 2 nm in the bulk of the well. For the numerical evaluation, the Dirac delta function $\delta$ is approximated by a Gaussian distribution with a broadening parameter $\sigma = 5$ meV. Finally, the LDOS is evaluated at the bulk Dirac-point energy ($E_D = 0.036$ eV).

For thin films, the finite-size effects induce a coupling between the top and bottom surface states. This coupling lifts their degeneracy, resulting in two distinct, well-separated Fermi-arc-like contours, as seen in Figs. 14(a)–14(e). As the film thickness $L_z$ increases, the spatial overlap between the wave functions at opposite surfaces decreases, and the two contours gradually merge.

To quantify this intersurface coupling, Fig. 14(f) plots $\Delta k_x$, the momentum separation between the two arcs evaluated at $k_z = 0$. The decay of $\Delta k_x$ as a function of thickness is well captured by an analytical model of the form $\Delta k_x = A \exp(-L_z/L_0)$. This exponential dependency accurately reflects the asymptotic decay of surface states as they penetrate into the bulk of the material. Extrapolating this model to a thicker slab of $L_z = 35$ nm yields a negligible momentum separation of $\Delta k_x \approx 1.45 \times 10^{-4}$ Å$^{-1}$, confirming that the opposite surfaces are effectively decoupled at this scale.

Finally, Fig. 15 illustrates the evolution of the crossing point of the Fermi-arc-like contours in $(1\bar{1}00)$ films with increasing thickness. As the finite-size effects diminish, this surface state crossing point converges toward $k_D$, the wave vector of the bulk Dirac point.

### 3. Fermi-arc-like contours in $(11\bar{2}0)$ films

Figure 16 shows the evolution of the surface LDOS in $(11\bar{2}0)$ films. As for the $(1\bar{1}00)$ orientation, the two split Fermi-arc-like contours gradually merge as the film thickness increases. Figure 17 shows that their crossing point at $k_x = 0$ approaches the projected bulk Dirac wave vector $k_D$. These results confirm that the Fermi-arc-like surface states persist for another confinement direction perpendicular to the $c$ axis.

[1] S. M. Young, S. Zaheer, J. C. Y. Teo, C. L. Kane, E. J. Mele, and A. M. Rappe, Dirac semimetal in three dimensions, Phys. Rev. Lett. **108**, 140405 (2012).

[2] Z. Wang, Y. Sun, X.-Q. Chen, C. Franchini, G. Xu, H. Weng, X. Dai, and Z. Fang, Dirac semimetal and topological phase transitions in $A_3$Bi ($a$ = Na, K, Rb), Phys. Rev. B **85**, 195320 (2012).

[3] A. H. Castro Neto, F. Guinea, N. M. R. Peres, K. S. Novoselov, and A. K. Geim, The electronic properties of graphene, Rev. Mod. Phys. **81**, 109 (2009).

[4] M. Z. Hasan and C. L. Kane, *Colloquium*: Topological insulators, Rev. Mod. Phys. **82**, 3045 (2010).

[5] X.-L. Qi and S.-C. Zhang, Topological insulators and superconductors, Rev. Mod. Phys. **83**, 1057 (2011).

[6] Z. Wang, H. Weng, Q. Wu, X. Dai, and Z. Fang, Three-dimensional Dirac semimetal and quantum transport in $Cd_3As_2$, Phys. Rev. B **88**, 125427 (2013).

[7] Z. K. Liu, B. Zhou, Y. Zhang, Z. J. Wang, H. M. Weng, D. Prabhakaran, S.-K. Mo, Z. X. Shen, Z. Fang, X. Dai, Z. Hussain, and Y. L. Chen, Discovery of a three-dimensional topological Dirac semimetal, $Na_3Bi$, Science **343**, 864 (2014).

[8] S.-Y. Xu, C. Liu, S. K. Kushwaha, R. Sankar, J. W. Krizan, I. Belopolski, M. Neupane, G. Bian, N. Alidoust, T.-R. Chang, H.-T. Jeng, C.-Y. Huang, W.-F. Tsai, H. Lin, P. P. Shibayev, F.-C. Chou, R. J. Cava, and M. Z. Hasan, Observation of Fermi arc surface states in a topological metal, Science **347**, 294 (2015).

[9] Z. K. Liu, J. Jiang, B. Zhou, Z. J. Wang, Y. Zhang, H. M. Weng, D. Prabhakaran, S.-K. Mo, H. Peng, P. Dudin, T. Kim, M. Hoesch, Z. Fang, X. Dai, Z. X. Shen, D. L. Feng, Z. Hussain, and Y. L. Chen, A stable three-dimensional topological Dirac semimetal $Cd_3As_2$, Nat. Mater. **13**, 677 (2014).

[10] S. Jeon, B. B. Zhou, A. Gyenis, B. E. Feldman, I. Kimchi, A. C. Potter, Q. D. Gibson, R. J. Cava, A. Vishwanath, and A. Yazdani, Landau quantization and quasiparticle interference in the three-dimensional Dirac semimetal $Cd_3As_2$, Nat. Mater. **13**, 851 (2014).

[11] M. Neupane, S.-Y. Xu, R. Sankar, N. Alidoust, G. Bian, C. Liu, I. Belopolski, T.-R. Chang, H.-T. Jeng, H. Lin, A. Bansil, F. Chou, and M. Z. Hasan, Observation of a three-dimensional topological Dirac semimetal phase in high-mobility $Cd_3As_2$, Nat. Commun. **5**, 3786 (2014).

[12] H. Zheng, S.-Y. Xu, G. Bian, C. Guo, G. Chang, D. S. Sanchez, I. Belopolski, C.-C. Lee, S.-M. Huang, X. Zhang, *et al.*, Atomic-scale visualization of quantum interference on a Weyl semimetal surface by scanning tunneling microscopy, ACS Nano **10**, 1378 (2016).

[13] J. Xiong, S. K. Kushwaha, T. Liang, J. W. Krizan, M. Hirschberger, W. Wang, R. J. Cava, and N. P. Ong, Evidence for the chiral anomaly in the Dirac semimetal $Na_3Bi$, Science **350**, 413 (2015).

[14] B.-J. Yang and N. Nagaosa, Classification of stable three-dimensional Dirac semimetals with nontrivial topology, Nat. Commun. **5**, 4898 (2014).

[15] N. P. Armitage, E. J. Mele, and A. Vishwanath, Weyl and Dirac semimetals in three-dimensional solids, Rev. Mod. Phys. **90**, 015001 (2018).

[16] C.-X. Liu, H. Zhang, B. Yan, X.-L. Qi, T. Frauenheim, X. Dai, Z. Fang, and S.-C. Zhang, Oscillatory crossover from two-dimensional to three-dimensional topological insulators, Phys. Rev. B **81**, 041307 (2010).

[17] C. Lyi and Y. Kim, Strain-driven higher-order topological Dirac semimetal in noncentrosymmetric $\gamma$-GeSe, Nano Lett. **25**, 6592 (2025).

[18] H. Pan, M. Wu, Y. Liu, and S. A. Yang, Electric control of topological phase transitions in Dirac semimetal thin films, Sci. Rep. **5**, 14639 (2015).

[19] J. L. Collins, A. Tadich, W. Wu, L. C. Gomes, J. N. B. Rodrigues, C. Liu, J. Hellerstedt, H. Ryu, S. Tang, S.-K. Mo, S. Adam, S. A. Yang, M. S. Fuhrer, and M. T. Edmonds, Electric-field-tuned topological phase transition in ultrathin $Na_3Bi$, Nature (London) **564**, 390 (2018).

[20] H. Xia, Y. Li, M. Cai, L. Qin, N. Zou, L. Peng, W. Duan, Y. Xu, W. Zhang, and Y.-S. Fu, Dimensional crossover and topological phase transition in Dirac semimetal $Na_3Bi$ films, ACS Nano **13**, 9647 (2019).

[21] M. Uchida, Y. Nakazawa, S. Nishihaya, K. Akiba, M. Kriener, Y. Kozuka, A. Miyake, Y. Taguchi, M. Tokunaga, N. Nagaosa, Y. Tokura, and M. Kawasaki, Quantum Hall states observed in thin films of Dirac semimetal $Cd_3As_2$, Nat. Commun. **8**, 2274 (2017).

[22] T. Schumann, L. Galletti, D. A. Kealhofer, H. Kim, M. Goyal, and S. Stemmer, Observation of the quantum Hall effect in confined films of the three-dimensional Dirac semimetal $Cd_3As_2$, Phys. Rev. Lett. **120**, 016801 (2018).

[23] C. Zhang, Y. Zhang, X. Yuan, S. Lu, J. Zhang, A. Narayan, Y. Liu, H. Zhang, Z. Ni, R. Liu, E. S. Choi, A. Suslov, S. Sanvito, L. Pi, H.-Z. Lu, A. C. Potter, and F. Xiu, Quantum Hall effect based on Weyl orbits in $Cd_3As_2$, Nature (London) **565**, 331 (2019).

[24] C. Fang, M. J. Gilbert, X. Dai, and B. A. Bernevig, Multi-Weyl topological semimetals stabilized by point group symmetry, Phys. Rev. Lett. **108**, 266802 (2012).

[25] H. Weng, C. Fang, Z. Fang, B. A. Bernevig, and X. Dai, Weyl semimetal phase in noncentrosymmetric transition-metal monophosphides, Phys. Rev. X **5**, 011029 (2015).

[26] S.-Y. Xu, I. Belopolski, N. Alidoust, M. Neupane, G. Bian, C. Zhang, R. Sankar, G. Chang, Z. Yuan, C.-C. Lee, *et al.*, Discovery of a Weyl fermion semimetal and topological Fermi arcs, Science **349**, 613 (2015).

[27] B. Q. Lv, H. M. Weng, B. B. Fu, X. P. Wang, H. Miao, J. Ma, P. Richard, X. C. Huang, L. X. Zhao, G. F. Chen, Z. Fang, X. Dai, T. Qian, and H. Ding, Experimental discovery of Weyl semimetal TaAs, Phys. Rev. X **5**, 031013 (2015).

[28] N. Xu, H. M. Weng, B. Q. Lv, C. E. Matt, J. Park, F. Bisti, V. N. Strocov, D. Gawryluk, E. Pomjakushina, K. Conder, N. C. Plumb, M. Radovic, G. Autes, O. V. Yazyev, Z. Fang, X. Dai, T. Qian, J. Mesot, H. Ding, and M. Shi, Observation of Weyl nodes and Fermi arcs in tantalum phosphide, Nat. Commun. **7**, 11006 (2016).

[29] S.-Y. Xu, N. Alidoust, I. Belopolski, Z. Yuan, G. Bian, T.-R. Chang, H. Zheng, V. N. Strocov, D. S. Sanchez, G. Chang, *et al.*, Discovery of a Weyl fermion state with Fermi arcs in niobium arsenide, Nat. Phys. **11**, 748 (2015).

[30] D.-F. Xu, Y.-P. Du, Z. Wang, Y.-P. Li, X.-H. Niu, Q. Yao, D. Pavel, Z.-A. Xu, X.-G. Wan, and D.-L. Feng, Observation of Fermi arcs in non-centrosymmetric Weyl semi-metal candidate NbP, Chin. Phys. Lett. **32**, 107101 (2015).

[31] M. Kargarian, M. Randeria, and Y.-M. Lu, Are the surface Fermi arcs in Dirac semimetals topologically protected? Proc. Natl. Acad. Sci. USA **113**, 8648 (2016).

[32] H. Gao, J. Strockoz, M. Frakulla, J. W. F. Venderbos, and H. Weng, Noncentrosymmetric topological Dirac semimetals in three dimensions, Phys. Rev. B **103**, 205151 (2021).

[33] M. Sato, J. Bouaziz, S. Sumita, S. Kobayashi, I. Tateishi, S. Bluegel, A. Furusaki, and M. Hirayama, Ideal spin-orbit-free Dirac semimetal and diverse topological transitions in $Y_8CoIn_3$ family, Commun. Mater. **5**, 253 (2024).

[34] K. A. Sergeeva, H. Zhang, A. S. Portniagin, E. Bossavit, G. Mu, S. V. Kershaw, S. Ithurria, P. Guyot-Sionnest, S. Keuleyan, C.

Delerue, X. Tang, A. L. Rogach, and E. Lhuillier, The rise of HgTe colloidal quantum dots for infrared optoelectronics, Adv. Funct. Mater. **34**, 2405307 (2024).

[35] M. König, S. Wiedmann, C. Brüne, A. Roth, H. Buhmann, L. W. Molenkamp, X.-L. Qi, and S.-C. Zhang, Quantum spin Hall insulator state in HgTe quantum wells, Science **318**, 766 (2007).

[36] C. Brüne, C. X. Liu, E. G. Novik, E. M. Hankiewicz, H. Buhmann, Y. L. Chen, X. L. Qi, Z. X. Shen, S. C. Zhang, and L. W. Molenkamp, Quantum Hall effect from the topological surface states of strained bulk HgTe, Phys. Rev. Lett. **106**, 126803 (2011).

[37] A. S. Portniagin, K. A. Sergeeva, S. V. Kershaw, and A. L. Rogach, Cation-exchange-derived wurtzite HgTe nanorods for sensitive photodetection in the short-wavelength infrared range, Chem. Mater. **35**, 5631 (2023).

[38] K. A. Sergeeva, A. S. Portniagin, D. Mastrippolito, C. Gureghian, A. Hage, D. De Pesseroey, M. Paye, E. Bossavit, A. A. Sergeev, Z. Li, *et al.*, Confining metastable wurtzite HgTe for infrared optoelectronics, ACS Nano **20**, 10686 (2026).

[39] P. E. Blöchl, Projector augmented-wave method, Phys. Rev. B **50**, 17953 (1994).

[40] J. P. Perdew, K. Burke, and M. Ernzerhof, Generalized gradient approximation made simple, Phys. Rev. Lett. **77**, 3865 (1996).

[41] A. V. Krukau, O. A. Vydrov, A. F. Izmaylov, and G. E. Scuseria, Influence of the exchange screening parameter on the performance of screened hybrid functionals, J. Chem. Phys. **125**, 224106 (2006).

[42] G. Kresse and J. Hafner, *Ab initio* molecular dynamics for liquid metals, Phys. Rev. B **47**, 558 (1993).

[43] G. Kresse and J. Furthmüller, Efficient iterative schemes for *ab initio* total-energy calculations using a plane-wave basis set, Phys. Rev. B **54**, 11169 (1996).

[44] G. Kresse and J. Furthmüller, Efficiency of *ab-initio* total energy calculations for metals and semiconductors using a plane-wave basis set, Comput. Mater. Sci. **6**, 15 (1996).

[45] G. Kresse and D. Joubert, From ultrasoft pseudopotentials to the projector augmented-wave method, Phys. Rev. B **59**, 1758 (1999).

[46] J. Gao, Q. Wu, C. Persson, and Z. Wang, Irvsp: To obtain irreducible representations of electronic states in the VASP, Comput. Phys. Commun. **261**, 107760 (2021).

[47] A. P. Cracknell, B. L. Davies, S. C. Miller, and W. F. Love, *General Introduction and Tables of Irreducible Representations of Space Groups* (IFI/Plenum, New York, 1979).

[48] L. Elcoro, B. Bradlyn, Z. Wang, M. G. Vergniory, J. Cano, C. Felser, B. A. Bernevig, D. Orobengoa, G. d. l. Flor, and M. I. Aroyo, Double crystallographic groups and their representations on the Bilbao crystallographic server, J. Appl. Cryst. **50**, 1457 (2017).

[49] G. H. Wannier, The structure of electronic excitation levels in insulating crystals, Phys. Rev. **52**, 191 (1937).

[50] G. Pizzi, V. Vitale, R. Arita, S. Blügel, F. Freimuth, G. Géranton, M. Gibertini, D. Gresch, C. Johnson, T. Koretsune, *et al.*, Wannier90 as a community code: New features and applications, J. Phys.: Condens. Matter **32**, 165902 (2020).

[51] C. Delerue and M. Lannoo, *Nanostructures: Theory and modeling* (Springer, Berlin, 2004).

[52] Y. M. Niquet, C. Delerue, G. Allan, and M. Lannoo, Method for tight-binding parametrization: Application to silicon nanostructures, Phys. Rev. B **62**, 5109 (2000).

[53] J.-M. Jancu, R. Scholz, F. Beltram, and F. Bassani, Empirical spds* tight-binding calculation for cubic semiconductors: General method and material parameters, Phys. Rev. B **57**, 6493 (1998).

[54] G. Allan, Y. M. Niquet, and C. Delerue, Quantum confinement energies in zinc-blende III–V and group IV semiconductors, Appl. Phys. Lett. **77**, 639 (2000).

[55] A. Hage and C. Delerue, Unusual optoelectronic and topological properties of HgTe nanocrystals, Phys. Rev. B **113**, 205430 (2026).

[56] G. Bastard and J. Brum, Electronic states in semiconductor heterostructures, IEEE J. Quantum Electron. **22**, 1625 (1986).

[57] Y. Wu, N. H. Jo, L.-L. Wang, C. A. Schmidt, K. M. Neilson, B. Schrunk, P. Swatek, A. Eaton, S. L. Bud'ko, P. C. Canfield, and A. Kaminski, Fragility of Fermi arcs in Dirac semimetals, Phys. Rev. B **99**, 161113 (2019).

[58] A.-Q. Wang, T.-Y. Zhao, C. Li, A. Brinkman, C.-G. Chu, and Z.-M. Liao, From surface Fermi arcs to Fermi loops in the Dirac semimetal $Cd_3As_2$, arXiv:2502.07499.

[59] J. C. Slater and G. F. Koster, Simplified LCAO method for the periodic potential problem, Phys. Rev. **94**, 1498 (1954).

[60] Y. M. Niquet, D. Rideau, C. Tavernier, H. Jaouen, and X. Blase, Onsite matrix elements of the tight-binding Hamiltonian of a strained crystal: Application to silicon, germanium, and their alloys, Phys. Rev. B **79**, 245201 (2009).

[61] G. Fishman, *Semi-Conducteurs: Les Bases de la Théorie K.P* (Editions de l'Ecole Polytechnique, Palaiseau, 2010).